New analytical expressions of the Rossiter-McLaughlin effect adapted to different observation techniques

Gwenaël Boué[1,2,3], Marco Montalto[1], Isabelle Boisse[1], Mahmoudreza Oshagh[1,4], and Nuno C. Santos[1,4]

[1] Centro de Astrofísica, Universidade do Porto, Rua das Estrelas, 4150-762 Porto, Portugal
[2] Astronomie et Systèmes Dynamiques, IMCCE-CNRS UMR8028, Observatoire de Paris, UPMC, 77 Av. Denfert-Rochereau, 75014 Paris, France
[3] Department of Astronomy and Astrophysics, University of Chicago, 5640 South Ellis Avenue, Chicago, IL 60637, USA
   e-mail: boue@oddjob.uchicago.edu
[4] Departamento de Física e Astronomia, Faculdade de Ciências, Universidade do Porto, Rua do Campo Alegre, 4169-007 Porto, Portugal

ABSTRACT

The Rossiter-McLaughlin (hereafter RM) effect is a key tool for measuring the projected spin-orbit angle between stellar spin axes and orbits of transiting planets. However, the measured radial velocity (RV) anomalies produced by this effect are not intrinsic and depend on both instrumental resolution and data reduction routines. Using inappropriate formulas to model the RM effect introduces biases, at least in the projected velocity $V \sin i_\star$ compared to the spectroscopic value. Currently, only the iodine cell technique has been modeled, which corresponds to observations done by, e.g., the HIRES spectrograph of the Keck telescope. In this paper, we provide a simple expression of the RM effect specially designed to model observations done by the Gaussian fit of a cross-correlation function (CCF) as in the routines performed by the HARPS team. We derived also a new analytical formulation of the RV anomaly associated to the iodine cell technique. For both formulas, we modeled the subplanet mean velocity v_p and dispersion β_p accurately taking the rotational broadening on the subplanet profile into account. We compare our formulas adapted to the CCF technique with simulated data generated with the numerical software SOAP-T and find good agreement up to $V \sin i_\star \lesssim 20$ km.s^{-1}. In contrast, the analytical models simulating the two different observation techniques can disagree by about 10σ in $V \sin i_\star$ for large spin-orbit misalignments. It is thus important to apply the adapted model when fitting data.

Key words. Astronomical instrumentation, methods and techniques – Instrumentation: spectrographs – Methods: analytical – Methods: data analysis – Methods: numerical – Techniques: spectroscopic – Planetary systems – Planets and satellites: fundamental parameters – Planets and satellites: general – Stars: planetary systems

1. Introduction

Transiting planets produce radial velocity (RV) anomalies when crossing the disk of their star. This mechanism, known as the Rossiter-McLaughlin effect (hereafter RM effect), is due to the stellar proper rotation and the fact that during a transit, a planet successively covers different portions of the stellar disk with different average velocities along the line of sight (Holt 1893; Rossiter 1924; McLaughlin 1924). The RM effect has gained importance in the exoplanet community since it allows the measurement of the projected angle between the stellar spin-axis and the orbit of the planet.

The first measurements of the RM effect induced by a transiting planet were performed almost simultaneously with two different instruments on the same bright star HD209458. Queloz et al. (2000) observed the signal with the ELODIE spectrograph on the 193cm telescope of the Observatoire de Haute Provence, while Bundy & Marcy (2000) used the HIRES spectrograph on the Keck telescope. As explained later on, the choice of the instrument and, more particularly, the subsequent reduction analysis, have a non negligible impact on the resulting shape of signal. It is thus interesting to see that the two kinds of instrument, coupled with their own data treatment, which are still employed today, have been used in parallel since the beginning.

The first planet-host stars studied with this technique were all compatible with low obliquity. It was along the lines of the model of planet migration in a protoplanetary disk. But then, several misaligned systems have been detected, starting with XO-3 with an angle initially announced at 70° ± 15° (Hébrard et al. 2008) and then refined to 37.3° ± 3° (Winn et al. 2009), yet still significantly misaligned. With the growth of the sample, a first correlation appeared showing that the hottest stars tend to be more misaligned (Winn et al. 2010). Additionally, a first statistical comparison between observations and theoretical predictions have been performed (Triaud et al. 2010), suggesting that some of the hot Jupiters might be the result of the interaction with a stellar companion, leading to a Lidov-Kozai mechanism, characterized by phases of large eccentricity and inclination and followed by a circularization by tides raised on the planet as it approaches the star (Wu & Murray 2003; Fabrycky & Tremaine 2007). Other scenarios have then been developed to explain the formation of hot Jupiters, such as planet-planet scattering (Rasio & Ford 1996; Beaugé & Nesvorný 2012), the crossing of secular resonances (Wu & Lithwick 2011), or the Lidov-Kozai mechanism produced by a planetary companion (Naoz et al. 2011; Nagasawa & Ida 2011). A new trend between age and obliquity has also been found, suggesting that tidal dissipation may play an important role in the evolution of those systems (Triaud 2011).

Accurate modelings of the RM effect are thus needed to get reliable information on the current obliquity of stars and to test theoretical predictions. In the literature, one can find several

analytical expressions to model this effect (Kopal 1942; Ohta et al. 2005; Giménez 2006; Hirano et al. 2010, 2011). They are not all identical because they model different techniques of radial velocity measurements.

This raises an issue that should be considered with caution. RVs measured by different techniques or even by different instruments using the same algorithm can differ by more than a constant offset. To illustrate this point, we consider a random variable with a given probability distribution function (PDF), and ask what its *average* value is. The term *average* is vague and can mean different quantities: mean, median, mode, etc. Nevertheless, if the PDF is symmetrical, any of these quantities lead to the same result, eventually with different robustnesses with respect to noise. But if the PDF is *not* symmetrical, each estimator of the *average* value provides different results that cannot be compared directly. The situation is similar in RV observations, as noticed by Hirano et al. (2010). There are at least two different ways to measure RVs. One relies on the iodine cell technique which consists in fitting an observed spectrum with a modeled one that is Doppler-shifted (Butler et al. 1996). The other is based on a Gaussian fit to a cross-correlation function (CCF) (Baranne et al. 1996; Pepe et al. 2002). The former technique is applied to observations made with HIRES on the Keck telescope or with HDS at the Subaru telescope, while the latter is the routine of, e.g., SOPHIE at the Observatoire de Haute Provence or HARPS at La Silla Observatory. If stars are affected by neither spots nor transiting planets, their spectral lines have constant shapes, and thus the RVs derived by any instruments may only differ by a constant offset. In contrast, spectral lines are deformed during transits, and these deformations vary with time. As a consequence, each analysis routine is expected to lead to a different signal. In turn, it is important to have an analytical model adapted to each analysis routine in order to interpret RM data. Moreover, it also means that one should not combine RM measurements from different instruments.

The first analytical expressions of the RM effect were derived by Kopal (1942), Ohta et al. (2005), and Giménez (2006). They all computed the weighted mean velocity, hereafter called v_{mean}, along the line of sight of the stellar surface uncovered by the planet. This mean velocity, weighted by the surface intensity, leads to an exact expression of the form

$$v_{\mathrm{mean}} = -\frac{f}{1-f} v_p \,, \tag{1}$$

where f is the fraction of the flux blocked by the planet disk and v_p is the average velocity of the surface of the star covered by the planet. This expression is simple and exact. There is no assumption behind it. But, it does not correspond to the quantity that is actually measured in the observations by either the iodine cell technique, or by the Gaussian fit of the CCF. Thus, the analytical prediction v_{mean} is systematically biased when compared directly with observations. The difference increases for high stellar rotational velocities.

To solve this problem, Hirano et al. (2010) propose a new analytical expression closely related to the reduction algorithm of the iodine cell technique (see Fig. 1). This method consists in fitting a shifted spectrum outside of transits, which is modeled, here, by a single averaged spectral line and noted[1] $\mathcal{F}_{\mathrm{star}}(v - \bar{v})$, with the line profile detected during a transit $\mathcal{F}_{\mathrm{transit}}(v)$, via the Doppler shift $\bar{v}$. The quantity provided by the formulas of Hirano

et al. (2010) is the value, hereafter denoted v_{H10}, of the velocity $\bar{v}$ that maximizes the cross-correlation between the two line profiles $C(\bar{v}) = \int \mathcal{F}_{\mathrm{star}}(v - \bar{v}) \mathcal{F}_{\mathrm{transit}}(v)\, dv$. We show in Sect. 3.1 that if $\mathcal{F}_{\mathrm{star}}$ is an even function, the maximization of the cross-correlation $C(\bar{v})$ is indeed identical to the minimization of the chi-square associated to the fit of $\mathcal{F}_{\mathrm{transit}}(v)$ by $\mathcal{F}_{\mathrm{star}}(v - \bar{v})$. In that case, the result depends on the actual shape of the line profiles, as observed in practice. In the simplest case where the line profiles of both the nonrotating and the rotating star are Gaussian, this method leads to (Hirano et al. 2010)

$$v_{\mathrm{H10}} = -\left(\frac{2\beta_\star^2}{\beta_\star^2 + \beta_p^2}\right)^{3/2} f v_p \left(1 - \frac{v_p^2}{2(\beta_\star^2 + \beta_p^2)}\right) \,, \tag{2}$$

where $\beta_\star$ and β_p are the dispersion of the Gaussian profiles $\mathcal{F}_{\mathrm{star}}(v)$ and $\mathcal{F}_{\mathrm{pla}}(v - v_p)$ respectively[2]. $\mathcal{F}_{\mathrm{pla}}(v - v_p)$ is the line profile of the light blocked by the planet centered on v_p. Although this expression is the result of an expansion in both f and v_p, it gives a better representation of the measured radial velocity. Hirano et al. (2010) also provide more complex expressions in the case of Voigt profiles, and in Hirano et al. (2011), additional effects are taken into account such as macro-turbulence. But the result is not expressed as a simple analytical formula and it requires several numerical integrations.

The model of Hirano et al. (2010, 2011) is well adapted to the iodine cell technique, but it still does not correspond to the analysis routines used on stabilized spectrographs, e.g., SOPHIE and HARPS (Baranne et al. 1996; Pepe et al. 2002). In these routines, the observed spectrum is first cross-correlated with a template spectrum. This gives the so-called cross-correlation function (CCF) which can be seen as a weighted average of all the spectral lines convolved with a rectangular function. Finally, the CCF is fitted by a Gaussian whose mean represents the observed radial velocity v_{CCF} (see Fig. 1). Currently, there is no analytical expression of this quantity in the literature. The goal of this paper is to provide such an expression. As we will see, even in the general case where the spectral line profile $\mathcal{F}_{\mathrm{star}}$ is not Gaussian, the resulting formula is as simple as Eq. (2) derived by Hirano et al. (2010) and exact in v_p.

This paper is organized as follows. In Sect. 2, we analytically derive an unbiased expression v_{CCF} modeling the RM effect as measured by, e.g., SOPHIE and HARPS. This formula is specially designed to simulate the radial velocity measurements obtained by fitting a Gaussian to a CCF. We first provide very generic expressions that relies only on the symmetry of the spectroscopic lines, and then, we give a much simpler formula corresponding to Gaussian subplanet line profiles. In Sect. 3, we propose a new expression v_{iodine} of the RM signal derived by the iodine technique. In comparison to the previous ones, it is analytical and valid for any spectroscopic $V \sin i_\star$. Then, in Sect. 4, we detail the calculation of the parameters entering into our formulas v_{CCF} and v_{iodine}, which are the flux fraction f occulted by the planet, the subplanet velocity v_p, and the dispersion β_p. In Sect. 5, we compare our analytical results with simulated data generated with SOAP-T, a modified version of the numerical code SOAP (Boisse et al. 2012), able to reproduce RM signals (Oshagh et al. 2012). We also analyze biases introduced by the application of a wrong model in the fit of RM signals. Finally, we conclude in Sect. 6.

---

[1] Here, and throughout the paper, the line profiles are expressed as a function of radial velocity v, instead of wavelength.

[2] In this paper, unit Gaussians are defined by $\mathcal{G}_\sigma(v) = (\sqrt{2\pi}\sigma)^{-1} \exp(-v^2/(2\sigma^2))$, while in (Hirano et al. 2010), they are defined by $\mathcal{G}_{\tilde{\sigma}}(v) = (\sqrt{\pi}\tilde{\sigma})^{-1} \exp(-v^2/\tilde{\sigma}^2)$. There is thus a difference of a factor 2 in the parenthesis of Eq. (2) with respect to (Hirano et al. 2010, Eq. 36).
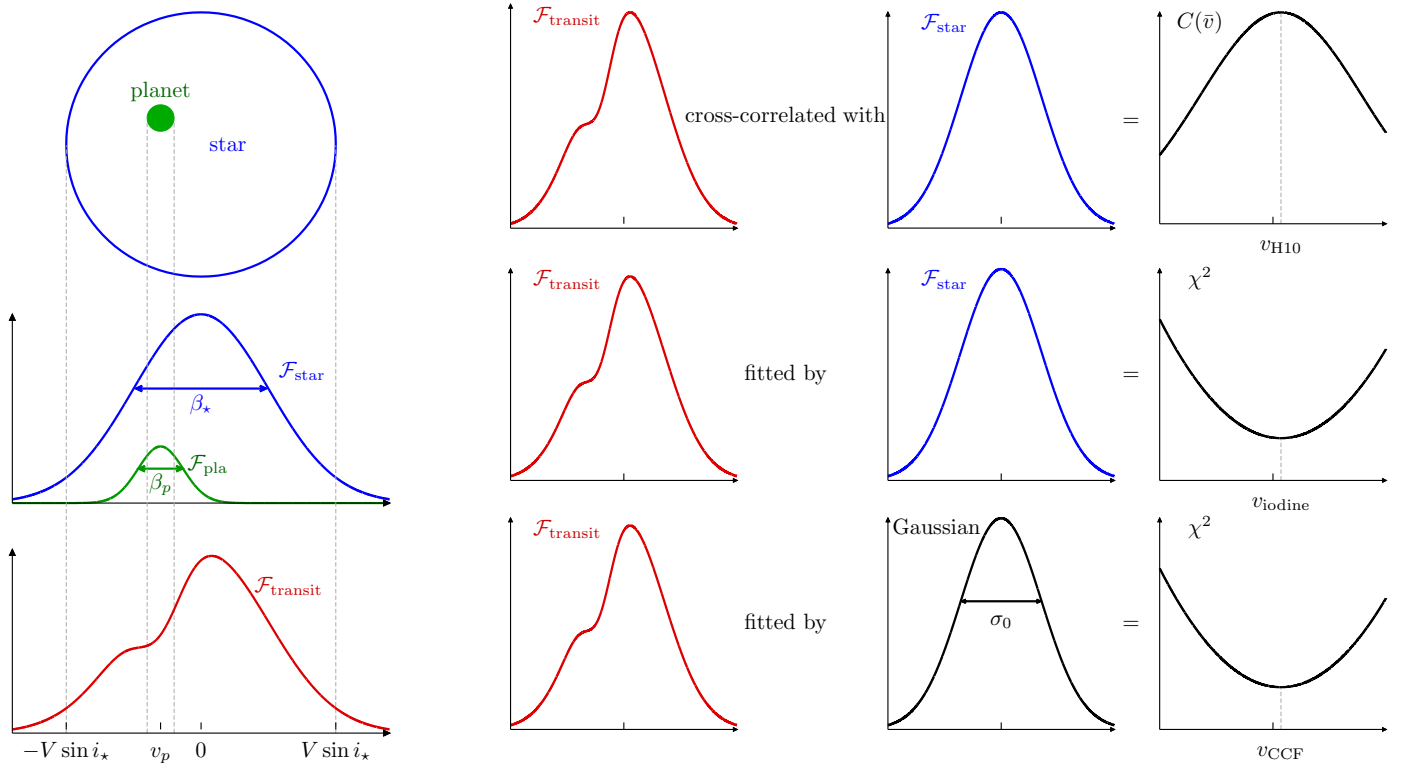
Fig. 1. Simplified illustration of different methods to compute the Rossiter-McLaughlin effect. v_{H10}, v_{iodine}, and v_{CCF} represent the result of the hypothesis made in Hirano et al. (2010), the result of the data reduction done with the iodine cell technique, and the result of the data reduction done with the CCF technique, respectively.

2. Modeling of the RM effect measured by the CCF technique

2.1. General derivation

We derive a very general expression of the RM effect obtained using a Gaussian fit to the CCF. As in Hirano et al. (2010), we only consider the linear effect with respect to the flux ratio f. But the method can easily be generalized to higher orders. We define $\mathcal{F}_{star}(v)$, $\mathcal{F}_{pla}(v - v_p)$, and $\mathcal{F}_{transit}(v)$ the line profile of the CCF produced by the integrated stellar surface, by the part of the stellar surface covered by the planet, and by the uncovered stellar surface, respectively. At this stage, the line profiles $\mathcal{F}_{star}$, $\mathcal{F}_{pla}$, and $\mathcal{F}_{transit}$ are not necessarily Gaussian. The dependency of $\mathcal{F}_{pla}$ is on $(v - v_p)$ because this line is centered on v_p. By convention, $\mathcal{F}_{star}(v)$ and $\mathcal{F}_{pla}(v - v_p)$ are normalized to one. With this convention, even absorption spectral lines are *positive*. We have $\mathcal{F}_{transit}(v) = \mathcal{F}_{star}(v) - f\mathcal{F}_{pla}(v - v_p)$. Moreover, we denote $\mathcal{G}_\sigma(v)$ as the unit Gaussian profile with dispersion σ and centered on the origin

$$\mathcal{G}_\sigma(v) = \frac{1}{\sqrt{2\pi}\sigma} \exp\left(-\frac{v^2}{2\sigma^2}\right) . \tag{3}$$

The fit of the CCF measured during transit, $\mathcal{F}_{transit}(v)$, by a Gaussian corresponds to the maximization of the likelihood

$$\chi^2(a, \bar{v}, \sigma) = \int (\mathcal{F}_{transit}(v) - a\mathcal{G}_\sigma(v - \bar{v}))^2 \, dv \tag{4}$$

with respect to the normalization factor a, the mean velocity $\bar{v}$, and the dispersion σ. The partial derivatives read as

$$\frac{\partial \chi^2}{\partial a} = -2 \int \mathcal{G}_\sigma(v - \bar{v})(\mathcal{F}_{transit}(v) - a\mathcal{G}_\sigma(v - \bar{v})) \, dv \; ;$$

$$\frac{\partial \chi^2}{\partial \bar{v}} = -\frac{2a}{\sigma^2} \int (v - \bar{v})\mathcal{G}_\sigma(v - \bar{v})(\mathcal{F}_{transit}(v) - a\mathcal{G}_\sigma(v - \bar{v})) \, dv \; ;$$

$$\frac{\partial \chi^2}{\partial \sigma} = -\frac{2a}{\sigma^3} \int ((v - \bar{v})^2 - \sigma^2)\mathcal{G}_\sigma(v - \bar{v})(\mathcal{F}_{transit}(v) - a\mathcal{G}_\sigma(v - \bar{v})) \, dv.$$

$$\tag{5}$$

We now set all the derivatives to zero, express $\mathcal{F}_{transit}(v)$ as a function of $\mathcal{F}_{star}(v)$ and $\mathcal{F}_{pla}(v)$, and reorder the terms. The system of equations (5) is equivalent to

$$\int F(a, \bar{v}, \sigma; v) \, dv = f \int \mathcal{F}_{pla}(v - v_p)\mathcal{G}_\sigma(v - \bar{v}) \, dv \; ;$$

$$\int v F(a, \bar{v}, \sigma; v) \, dv = f \int v\mathcal{F}_{pla}(v - v_p)\mathcal{G}_\sigma(v - \bar{v}) \, dv \; ; \tag{6}$$

$$\int v^2 F(a, \bar{v}, \sigma; v) \, dv = f \int v^2\mathcal{F}_{pla}(v - v_p)\mathcal{G}_\sigma(v - \bar{v}) \, dv \; ,$$

with

$$F(a, \bar{v}, \sigma; v) = \mathcal{G}_\sigma(v - \bar{v})(\mathcal{F}_{star}(v) - a\mathcal{G}_\sigma(v - \bar{v})) . \tag{7}$$

To solve this system, we apply the usual perturbation method. We develop the parameters in series of the flux ratio f, i.e., $a = a_0 + f a_1 + f^2 a_2 + \ldots$, and idem for $\bar{v}$ and σ. At the zeroth order in f, the system (6) corresponds to the fit of $\mathcal{F}_{star}(v)$

by a Gaussian. The effect of the planet is absent from the fit, thus $\bar{v}_0 = 0$. The other parameters a_0 and σ_0 are those of the best Gaussian fit outside of transits.

In a second step, we linearize the system (6) in the vicinity of the zeroth order solution. We thus compute the partial derivatives of

$$M_n(a, \bar{v}, \sigma) = \int v^n F(a, \bar{v}, \sigma) \, dv , \tag{8}$$

appearing in the left-hand side of (6), at $a = a_0$, $\bar{v} = \bar{v}_0 = 0$, and $\sigma = \sigma_0$. To avoid fastidious calculation, we make the simple hypothesis that $\mathcal{F}_{star}(v)$ is symmetrical, or more precisely, an even function of the velocity v. In practice, due to the convective blue shift (CB), spectral lines are not perfectly symmetric. Nevertheless, the net effect of CB is to add a constant offset that does not modify RM signals (Albrecht et al. 2012). Then, $M_0(a, \bar{v}, \sigma)$ and $M_2(a, \bar{v}, \sigma)$ are even functions of $\bar{v}$, while $M_1(a, \bar{v}, \sigma)$ is odd. As a result, the derivatives $\partial M_0/\partial\bar{v}$, $\partial M_2/\partial\bar{v}$, $\partial M_1/\partial a$, and $\partial M_1/\partial\sigma$ taken at $\bar{v} = 0$ vanish. Moreover, if the subplanet line profile is also an even function then the integrals of the righthand side of the system (6) become simple convolutions at $\bar{v} = 0$. Then there is only

$$\left(\frac{\partial M_0}{\partial a}\right) a_1 + \left(\frac{\partial M_0}{\partial \sigma}\right) \sigma_1 = \left[\mathcal{G}_{\sigma_0} * \mathcal{F}_{pla}\right](v_p) ,$$

$$\left(\frac{\partial M_1}{\partial \bar{v}}\right) \bar{v}_1 \qquad\qquad = \left[(v\,\mathcal{G}_{\sigma_0}) * \mathcal{F}_{pla}\right](v_p) , \tag{9}$$

$$\left(\frac{\partial M_2}{\partial a}\right) a_1 + \left(\frac{\partial M_2}{\partial \sigma}\right) \sigma_1 = \left[(v^2\mathcal{G}_{\sigma_0}) * \mathcal{F}_{pla}\right](v_p) ,$$

where $*$ denotes the convolution product. The first and the third lines are independent of the mean velocity $\bar{v}_1$. Their resolution provides a correction to the amplitude and the width of the best Gaussian fit during a transit. The second equation is the most interesting, since it contains the quantity $\bar{v}_1$ we are looking for. By chance, this is also the simplest. The velocity anomaly obtained by the Gaussian fit $v_{CCF} = \bar{v} = f\bar{v}_1$ is then

$$v_{CCF} = f \left(\frac{\partial M_1}{\partial \bar{v}}\right)^{-1} \left[(v\,\mathcal{G}_{\sigma_0}) * \mathcal{F}_{pla}\right](v_p) \tag{10}$$

where $\partial M_1/\partial\bar{v}$ should be computed at $(a_0, 0, \sigma_0)$, i.e.,

$$\frac{\partial M_1}{\partial \bar{v}} = \int \frac{v^2}{\sigma_0^2} \mathcal{G}_{\sigma_0}(v) \left(\mathcal{F}_{star}(v) - 2a_0 \mathcal{G}_{\sigma_0}(v)\right) \, dv$$
$$= -\frac{a_0}{4\sigma_0 \sqrt{\pi}} + \left[(v^2 \mathcal{G}_{\sigma_0}) * (\mathcal{F}_{star} - a_0 \mathcal{G}_{\sigma_0})\right](0) . \tag{11}$$

The convolution product taken at 0 on the righthand side of (11) is nothing else but M_2, which cancels by the definitions of a_0 and σ_0. Thus the RM effect now reads as

$$v_{CCF} = -\frac{4\sigma_0 \sqrt{\pi}}{a_0} f \left[(v\,\mathcal{G}_{\sigma_0}) * \mathcal{F}_{pla}\right](v_p) . \tag{12}$$

This expression does not depend directly on the stellar line profile $\mathcal{F}_{star}$. The dependence only occurs through the best Gaussian fit (a_0 and σ_0), which is performed to derive the radial velocity. The formula (12) is thus very powerful, since it does not require any knowledge on $\mathcal{F}_{star}$. Unfortunately, the amplitude a_0 of the best Gaussian fit in (12) is associated to a normalized line profile $\mathcal{F}_{star}$ while, in practice, the area of a CCF is difficult to measure,

and $\mathcal{F}_{star}$ is never normalized. We thus provide the expression of a_0 as a function of $\mathcal{F}_{star}$ and the best Gaussian fit $\mathcal{G}_{\sigma_0}$,

$$a_0 = \frac{\int \mathcal{G}_{\sigma_0}(v)\mathcal{F}_{star}(v) \, dv}{\int \mathcal{G}_{\sigma_0}(v)\mathcal{G}_{\sigma_0}(v) \, dv} = 2\sigma_0 \sqrt{\pi} \left[\mathcal{G}_{\sigma_0} * \mathcal{F}_{star}\right](0) . \tag{13}$$

We emphasize that a_0 is independent of v_p. As a consequence, it does not affect the shape of the RM effect, but only slightly the amplitude (a_0 remains close to one). The computation of a_0 is detailed in Appendix B.

2.2. Gaussian subplanet line profile

At this stage, the expression (12) is very general, and holds as long as the line profiles $\mathcal{F}_{star}(v)$ and $\mathcal{F}_{pla}(v)$ are symmetric.

We now make the hypothesis that the subplanet line profile $\mathcal{F}_{pla}(v)$ is Gaussian. It should be stressed that, as long as the planet radius is small compared to that of the star, the subplanet line profile is only weakly affected by the stellar rotation (see Sect. 4) and thus, it is well approximated by that of the non-rotating star, which we assume to be Gaussian. Then, the subplanet profile can be considered Gaussian, or equal to the sum of two Gaussians if macro-turbulence is taken into account (see Appendix A). We denote β_p as the width of the subplanet line profile, i.e., $\mathcal{F}_{pla}(v) = \mathcal{G}_{\beta_p}(v)$. In that case, the expression of the RM effect (12) becomes

$$v_{CCF} = -\frac{1}{a_0} \left(\frac{2\sigma_0^2}{\sigma_0^2 + \beta_p^2}\right)^{3/2} f v_p \exp\left(-\frac{v_p^2}{2(\sigma_0^2 + \beta_p^2)}\right) . \tag{14}$$

This is the main equation of this paper. It represents a good compromise between simplicity and accuracy for the modeling of RM signals measured by a Gaussian fit of the CCF.

2.3. Gaussian stellar line profile

For completeness, we give the expression in the case where the stellar line profile is a normalized Gaussian with dispersion $\beta_\star$. The best fit should give $a_0 = 1$ and $\sigma_0 = \beta_\star$. Then, we get

$$v_{CCF} = -\left(\frac{2\beta_\star^2}{\beta_\star^2 + \beta_p^2}\right)^{3/2} f v_p \exp\left(-\frac{v_p^2}{2(\beta_\star^2 + \beta_p^2)}\right) . \tag{15}$$

This formula is equivalent to v_{H10} (2) given by Hirano et al. (2010). More precisely, Eq. (2) is the beginning of the expansion of v_{CCF}. Indeed, if the stellar line profile is Gaussian, the two approaches are identical.

3. Modeling of the RM effect measured by the iodine cell technique

In this section, we first explain the equivalence between the iodine cell technique and the maximization of the cross-correlation $C(\bar{v})$ (Hirano et al. 2010, 2011). The aim is to emphasize the hypotheses behind this equivalence and, thus, to show its limitations. In a second step, we provide a general expression that models the iodine cell technique. It should be stressed that the function $C(\bar{v})$ is different from the CCF of the previous section and is not used in the same way. It involves the spectrum during transit and a modeled one without transit deformations. This function $C(\bar{v})$ is computed to provide the RV at its maximum. On the other hand, the CCF is the cross-correlation between the spectrum and a mask. The goal is to provide a single averaged line that is then fitted by a Gaussian curve.

3.1. Link between the iodine cell technique and the maximization of $C(\bar{v})$

The analysis routine based on the iodine cell technique involves a fit with 13 parameters of the observed spectrum by a modeled one that is Doppler-shifted (Butler et al. 1996). We assume that this can be approximated by the fit of a single parameter ($\bar{v}$) representing the Doppler shift between a modeled line profile $\mathcal{F}_{\text{star}}(v)$ and the observed one (here during a transit) $\mathcal{F}_{\text{transit}}(v)$. The chi-square of this fit reads

$$\chi^2(\bar{v}) = \int_{-\infty}^{+\infty} (\mathcal{F}_{\text{transit}}(v) - \mathcal{F}_{\text{star}}(v - \bar{v}))^2 \, dv . \quad (16)$$

The minimization of this chi-square corresponds to $d\chi^2/d\bar{v} = 0$ with

$$\frac{d\chi^2(\bar{v})}{d\bar{v}} = 2 \int \frac{d\mathcal{F}_{\text{star}}}{dv}(v - \bar{v})(\mathcal{F}_{\text{transit}}(v) - \mathcal{F}_{\text{star}}(v - \bar{v})) \, dv . \quad (17)$$

The integral on the righthand side can be split into the sum of two integrals

$$\frac{d\chi^2(\bar{v})}{d\bar{v}} = 2(I_1(\bar{v}) + I_2(\bar{v})) , \quad (18)$$

where the first one, $I_1(\bar{v})$, is the cross-correlation of $d\mathcal{F}_{\text{star}}/dv$ by $\mathcal{F}_{\text{transit}}$ taken at $\bar{v}$, while the other is, after the change of variable $u = v - \bar{v}$,

$$I_2 = \int_{-\infty}^{\infty} \frac{d\mathcal{F}_{\text{star}}}{dv}(u)\mathcal{F}_{\text{star}}(u) \, du . \quad (19)$$

If $\mathcal{F}_{\text{star}}$ is even, its derivative is odd, and thus the integral I_2 over $\mathbb{R}$ vanishes. In that case, only

$$\frac{d\chi^2(\bar{v})}{d\bar{v}} = 2 \left(\frac{d\mathcal{F}_{\text{star}}}{dv} \right) \star \mathcal{F}_{\text{transit}} \quad (20)$$

remains, where $\star$ denotes the cross-correlation product defined by

$$[f \star g](x) = \int_{-\infty}^{+\infty} f(y - x)g(y) \, dy . \quad (21)$$

We then use the property of the derivative of the cross-correlation of two functions

$$\frac{d}{dx}(f \star g) = -\frac{df}{dx} \star g = f \star \frac{dg}{dx} . \quad (22)$$

By identification, we obtain

$$\frac{d\chi^2(\bar{v})}{d\bar{v}} = -2 \frac{d}{d\bar{v}}(\mathcal{F}_{\text{star}} \star \mathcal{F}_{\text{transit}}) = -2 \frac{dC(\bar{v})}{d\bar{v}} , \quad (23)$$

where $C(\bar{v})$ is defined as in Hirano et al. (2010). Thus, the minimization of the chi-square involved in the iodine cell technique is indeed equivalent to the maximization of the cross-correlation $C(\bar{v})$ as computed in Hirano et al. (2010). This result holds as long as the complicated fit with 13 parameters can be modeled by the fit of the single parameter $\bar{v}$, and if the modeled line profile is symmetrical. The second condition may not be true in general. If the asymmetry is not too strong, the integral I_2 would be a small perturbation, and the result obtained by the maximization of the cross-correlation $C(\bar{v})$ should differ from the minimization of the chi-square by only a small constant.

3.2. General expression of the RM effect

To derive a general expression of the RV signal measured by the iodine technique, we use the same model as Hirano et al. (2010), which consists in maximizing $C(\bar{v})$ where

$$C(\bar{v}) = \int \mathcal{F}_{\text{star}}(v - \bar{v})[\mathcal{F}_{\text{star}}(v) - f\mathcal{F}_{\text{pla}}(v - v_p)] \, dv . \quad (24)$$

Then, the condition $dC(\bar{v})/d\bar{v} = 0$ leads to

$$\left[\frac{d\mathcal{F}_{\text{star}}}{dv} \star \mathcal{F}_{\text{star}} \right](\bar{v}) = f \int \frac{d\mathcal{F}_{\text{star}}}{dv}(v - \bar{v})\mathcal{F}_{\text{pla}}(v - v_p) \, dv . \quad (25)$$

As in the previous section, we expand $\bar{v}$ in series of f: $\bar{v} = \bar{v}_0 + f\bar{v}_1 + \dots$. At the zeroth order, we get

$$\left[\frac{d\mathcal{F}_{\text{star}}}{dv} \star \mathcal{F}_{\text{star}} \right](\bar{v}_0) = 0 . \quad (26)$$

If $\mathcal{F}_{\text{star}}(v)$ is an even function, this equality gives $\bar{v}_0 = 0$. Otherwise, $\bar{v}_0$ would be a small constant, depending only on the shape of the spectral lines, but not on v_p. Here, we assume that $\bar{v}_0 = 0$. At the first order in the flux ratio f, assuming that $\mathcal{F}_{\text{pla}}$ is even, we obtain, with $v_{\text{iodine}} = f\bar{v}_1$,

$$v_{\text{iodine}} = \frac{1}{A_0} f \left[\frac{d\mathcal{F}_{\text{star}}}{dv} * \mathcal{F}_{\text{pla}} \right](v_p) , \quad (27)$$

where

$$A_0 = \frac{d}{d\bar{v}} \left[\frac{d\mathcal{F}_{\text{star}}}{dv} \star \mathcal{F}_{\text{star}} \right]_{\bar{v}=0} = \int_{-\infty}^{+\infty} \left(\frac{d\mathcal{F}_{\text{star}}}{dv} \right)^2 \, dv . \quad (28)$$

This result is more complex than (12) because it involves the derivatives of the stellar line profile $\mathcal{F}_{\text{star}}$ instead of the derivatives of a best Gaussian fit $\mathcal{G}_{\sigma_0}$ which are analytical. Of course, if $\mathcal{F}_{\text{star}}$ is Gaussian, we retrieve the result of the previous section (see Sect. 2.3).

In Appendix C, we provide an analytical expression of the numerator of v_{iodine} (27) in the case where the subplanet line profile is Gaussian and for a general limb-darkening law.

4. Parameters of the subplanet line profile

The expressions of the RM effect (14) and (27) depend on the fraction f of the flux covered by the planet, the subplanet velocity v_p, and the dispersion β_p. There are two approaches to evaluate them. On the one hand, both the flux fraction f and the mean velocity v_p can be computed exactly as a series of Jacobi polynomials (Giménez 2006). This is useful in the case of binary transits where the occulting object is big. On the other hand, only the flux fraction f is derived exactly using analytical algorithms such as the one given by (Mandel & Agol 2002), while v_p and β_p are estimated assuming uniform intensity below the planet (Hirano et al. 2010, 2011). Then, if $(\bar{x}, \bar{y})$ are the averaged coordinates over the surface of the star covered by the planet, and normalized to the radius of the star, $v_p \approx \bar{x}V \sin i_\star$, while β_p is constant and represents the width β_0 of the nonrotating star line profile.

Here, we choose a compromise between the two approaches and take the slope and the curvature of the intensity below the planet into account. This gives a better estimate of v_p and β_p in comparison to the uniform subplanet intensity hypothesis. But also it turns out that the method provides a simple and accurate expression for the flux fraction f. Another advantage of this method is that it can be easily applied to more complex problems where the gravity-darkening or the tidal deformations of both the planet and the star are taken into account.

4.1. Method

To describe the method, we take the example of the computation of the flux fraction f. The expression of f reads as

$$f = \iint_{\mathcal{S}_p} I(x, y) \, dx \, dy \, , \tag{29}$$

where $\mathcal{S}_p$ is the surface of the stellar disk covered by the planet normalized by the square of the radius of the star. $I(x, y)$ is the normalized limb-darkening of the star expressed as a function of the normalized coordinates (x, y). For the moment, we do not need to give its expression.

A very rough approximation of f is obtained assuming uniform intensity below the planet. In that case, we obtain

$$f = I(\bar{x}, \bar{y}) \iint_{\mathcal{S}_p} dx \, dy \tag{30}$$

$$= I(\bar{x}, \bar{y}) \, \mathcal{S}_p \, ,$$

where

$$\bar{x} = \frac{1}{\mathcal{S}_p} \iint_{\mathcal{S}_p} x \, dx \, dy \, , \quad \text{and} \quad \bar{y} = \frac{1}{\mathcal{S}_p} \iint_{\mathcal{S}_p} y \, dx \, dy \, , \tag{31}$$

are the coordinates of the barycenter of the portion of the stellar disk covered by the planet. The formula (30) works well for very small planets but only during full transits (e.g. Mandel & Agol 2002). Close to the limb, the intensity $I(x, y)$ varies strongly with position and this approximation is not valid anymore. To overcome this issue, we propose to make an expansion of the limb-darkening profile $I(x, y)$ in the vicinity of $(\bar{x}, \bar{y})$. We get

$$\frac{f}{\mathcal{S}_p} = I(\bar{x}, \bar{y}) \langle 1 \rangle + J_x^{(0)} \langle x - \bar{x} \rangle + J_y^{(0)} \langle y - \bar{y} \rangle + \frac{1}{2} H_{xx}^{(0)} \left\langle (x - \bar{x})^2 \right\rangle$$

$$+ \frac{1}{2} H_{yy}^{(0)} \left\langle (y - \bar{y})^2 \right\rangle + H_{xy}^{(0)} \left\langle (x - \bar{x})(y - \bar{y}) \right\rangle \, , \tag{32}$$

where for any function $f(x, y)$,

$$\langle f(x, y) \rangle = \frac{1}{\mathcal{S}_p} \iint_{\mathcal{S}_p} f(x, y) \, dx \, dy \, , \tag{33}$$

where $J_x^{(0)} = \partial_x I(x, y)$ and $J_y^{(0)} = \partial_y I(x, y)$ are the components of the Jacobian of the surface intensity $I(x, y)$ computed at $(\bar{x}, \bar{y})$. Similarly, the components of the Hessian are

$$H_{xx}^{(0)} = \frac{\partial^2 I(x, y)}{\partial x^2} \, , \quad H_{yy}^{(0)} = \frac{\partial^2 I(x, y)}{\partial y^2} \, , \quad H_{xy}^{(0)} = \frac{\partial^2 I(x, y)}{\partial x \partial y} \, . \tag{34}$$

By construction, $\bar{x}$ and $\bar{y}$ are defined by $\bar{x} = \langle x \rangle$, and $\bar{y} = \langle y \rangle$. Thus, the linear terms in factor of the Jacobian $(J_x^{(0)}, J_y^{(0)})$ cancel in (32). At that point, only

$$\frac{f}{\mathcal{S}_p} = I(\bar{x}, \bar{y}) + \frac{1}{2} H_{xx}^{(0)} \left\langle (x - \bar{x})^2 \right\rangle + \frac{1}{2} H_{yy}^{(0)} \left\langle (y - \bar{y})^2 \right\rangle$$

$$+ H_{xy}^{(0)} \left\langle (x - \bar{x})(y - \bar{y}) \right\rangle \tag{35}$$

remains. The first term in (35) corresponds to the rough approximation derived in Eq. (30). The other terms provide a correction proportional to the square of the normalized planet radius $(r = R_p/R_\star)$ and are expected to be small.

4.2. Subplanet velocity

The above method applied to $I(x, y)$ to get the flux fraction f can be adapted to any other function. For example, the subplanet velocity is defined by

$$v_p = V \sin i_\star \frac{\iint_{\mathcal{S}_p} x I(x, y) \, dx \, dy}{\iint_{\mathcal{S}_p} I(x, y) \, dx \, dy} \, . \tag{36}$$

We denote $H_{xx}^{(1)}$, $H_{yy}^{(1)}$, and $H_{xy}^{(1)}$ as the components of the Hessian of $x I(x, y)$ at the averaged position $(\bar{x}, \bar{y})$ (31). Using the expression of f (35), at first order in r^2, we get

$$\frac{v_p}{V \sin i_\star} = \bar{x} + \frac{1}{2 I(\bar{x}, \bar{y})} \left(\left(H_{xx}^{(1)} - \bar{x} H_{xx}^{(0)} \right) \left\langle (x - \bar{x})^2 \right\rangle \right.$$

$$+ \left(H_{yy}^{(1)} - \bar{x} H_{yy}^{(0)} \right) \left\langle (y - \bar{y})^2 \right\rangle \tag{37}$$

$$\left. + 2 \left(H_{xy}^{(1)} - \bar{x} H_{xy}^{(0)} \right) \left\langle (x - \bar{x})(y - \bar{y}) \right\rangle \right) \, .$$

The denominator $I(\bar{x}, \bar{y})$ in (37), as well as the terms in $H_{xx}^{(0)}$, $H_{yy}^{(0)}$, and $H_{xy}^{(0)}$, come from the expansion of the denominator of (36).

4.3. Width of the subplanet line profile

The width of the subplanet line profile β_p is a combination of the width of the nonrotating line profile β_0 and a correction $\delta\beta_p$ due to the rotational broadening

$$\beta_p^2 = \beta_0^2 + \delta\beta_p^2 \, . \tag{38}$$

We define $\mathcal{V}_2$ as the average of the square of the subplanet velocity

$$\mathcal{V}_2 = (V \sin i_\star)^2 \frac{\iint_{\mathcal{S}_p} x^2 I(x, y) \, dx \, dy}{\iint_{\mathcal{S}_p} I(x, y) \, dx \, dy} \, . \tag{39}$$

With this notation, we have

$$\delta\beta_p^2 = \mathcal{V}_2 - v_p^2 \, . \tag{40}$$

Noting $H_{xx}^{(2)}$, $H_{yy}^{(2)}$, and $H_{xy}^{(2)}$, the components of the Hessian of $x^2 I(x, y)$ at the averaged coordinates $(\bar{x}, \bar{y})$, the expression of $\mathcal{V}_2$ reads as

$$\frac{\mathcal{V}_2}{(V \sin i_\star)^2} = \bar{x}^2 + \frac{1}{2 I(\bar{x}, \bar{y})} \left(\left(H_{xx}^{(2)} - \bar{x}^2 H_{xx}^{(0)} \right) \left\langle (x - \bar{x})^2 \right\rangle \right.$$

$$+ \left(H_{yy}^{(2)} - \bar{x}^2 H_{yy}^{(0)} \right) \left\langle (y - \bar{y})^2 \right\rangle \tag{41}$$

$$\left. + 2 \left(H_{xy}^{(2)} - \bar{x}^2 H_{xy}^{(0)} \right) \left\langle (x - \bar{x})(y - \bar{y}) \right\rangle \right) \, .$$

At first order, the $\bar{x}^2$ in $\mathcal{V}_2$ (39) cancels with the square of $\bar{x}$ in the expression of v_p (37). Thus, at first order, $\delta\beta_p$ vanishes and the width of the subplanet profile is equal to the width of the nonrotating star β_0. However, the quadratic terms do not cancel, and this provides an estimation of the contribution of the rotational broadening to the actual width of the subplanet profile.

Table 1. Second derivatives of $x^n I_\alpha(x,y)$, Eq. (42).

$$H_{xx}^{(n)} = n(n-1)x^{n-2}I_\alpha(x,y) - n(n+1)\,\alpha\, x^n I_{\alpha-2}(x,y)$$
$$\qquad + \alpha(\alpha-2)x^{n+2}I_{\alpha-4}(x,y)$$

$$H_{yy}^{(n)} = -n\alpha x^n I_{\alpha-2}(x,y) + \alpha(\alpha-2)x^n y^2 I_{\alpha-4}(x,y)$$

$$H_{xy}^{(n)} = -n\alpha x^{n-1}y I_{\alpha-2}(x,y) + \alpha(\alpha-2)x^{n+1}y^2 I_{\alpha-4}(x,y)$$
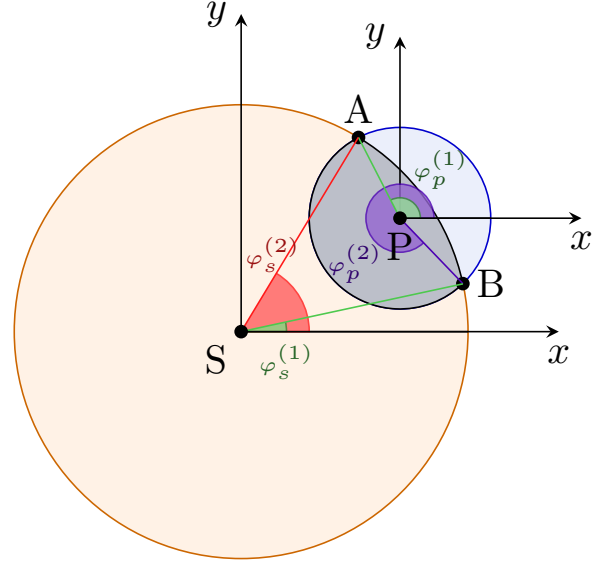

Fig. 2. Definition of the angles $\varphi_p^{(1)}$, $\varphi_p^{(2)}$, $\varphi_s^{(1)}$, and $\varphi_s^{(2)}$ during partial transit. The large circle centered on S represents the star, and the smaller one, centered on P, is the planet.

4.4. Limb-darkening and its derivatives

As we saw above, the determination of the subplanet profile depends on the limb-darkening law and its second derivatives. In this section, we provide generic formulas assuming that the limb-darkening law is a linear combination of functions $I_\alpha(x,y)$ defined by

$$I_\alpha(x,y) = \mu^\alpha = \left(1 - x^2 - y^2\right)^{\alpha/2}, \tag{42}$$

where $\mu = \sqrt{1-x^2-y^2}$ is the cosine of the angle between the normal of the stellar surface at (x,y) and the observer.

The second derivatives $H_{xx}^{(n)}$, $H_{yy}^{(n)}$, and $H_{xy}^{(n)}$ of $x^n I_\alpha(x,y)$ are given Table 1. These are the ones that are needed to compute the flux fraction f, the subplanet velocity v_p and the dispersion β_p. In practice, only the cases $n = 0, 1, 2$ are used.

From these general formulas, one can derive the expressions for the quadratic limb-darkening which reads as

$$I_q(x,y) = I_q(0)\left(1 - u_1(1-\mu) - u_2(1-\mu)^2\right) \tag{43}$$
$$\qquad = u_0' + u_1'\mu + u_2'\mu^2,$$

with $I_q(0)$ the central intensity such that $I_q(x,y)$ is normalized to one. By identification, we get

$$u_0' = \frac{1 - u_1 - u_2}{\pi(1 - u_1/3 - u_2/6)},$$

$$u_1' = \frac{u_1 + 2u_2}{\pi(1 - u_1/3 - u_2/6)}, \tag{44}$$

$$u_2' = \frac{-u_2}{\pi(1 - u_1/3 - u_2/6)}.$$

Equivalently, the so-called nonlinear limb-darkening is usually expressed as

$$I_{nl}(x,y) = I_{nl}(0)\left(1 - \sum_{n=1}^{4} c_n\left(1 - \mu^{n/2}\right)\right) \tag{45}$$
$$\qquad = c_0' + c_1'\mu^{1/2} + c_2'\mu + c_3'\mu^{3/2} + c_4'\mu^2,$$

with

$$c_0' = \frac{1 - c_1 - c_2 - c_3 - c_4}{\pi(1 - c_1/5 - c_2/3 - 3c_3/7 - c_4/2)}, \tag{46}$$

and for $1 \le n \le 4$,

$$c_n' = \frac{c_n}{\pi(1 - c_1/5 - c_2/3 - 3c_3/7 - c_4/2)}. \tag{47}$$

The normalizations in (44), (46), and (47) have been deduced from the integral of each $I_\alpha(x,y)$ over the entire disk of the star

$$\iint \mu^\alpha\, dx\, dy = \int_0^{2\pi} d\phi \int_0^{\pi/2} d\theta \, \cos^{\alpha+1}\theta \sin\theta = \frac{2\pi}{\alpha+2}. \tag{48}$$

4.5. Averaged coordinates and covariances

The last quantities that need to be computed in order to get the subplanet line profiles are the averaged coordinates $\langle x \rangle$, $\langle y \rangle$, the variances $\left\langle (x-\bar{x})^2 \right\rangle$, $\left\langle (y-\bar{y})^2 \right\rangle$, and the covariance $\langle (x-\bar{x})(y-\bar{y}) \rangle$. For that, we distinguish two cases.

4.5.1. During a full transit

In the case of a full transit, i.e., when the disk of the planet is fully inside the disk of the star, the problem gets simpler since the integrals (33) have to be computed over a uniform disk of area $S_p = \pi r^2$ and centered on the coordinates (x_0, y_0) of the planet. We get $(\bar{x}, \bar{y}) = (x_0, y_0)$, and

$$\left\langle (x-\bar{x})^2 \right\rangle = \left\langle (y-\bar{y})^2 \right\rangle = \frac{r^2}{4}, \tag{49}$$

$$\langle (x-\bar{x})(y-\bar{y}) \rangle = 0.$$

4.5.2. During ingress or egress

If the disk of the planet is crossing the limb of the star, the area where the integrals of the form (33) are computed is not circular (see the shaded area in Fig. 2). In that case, we use the very powerful method of Pál (2012), which gives expressions that also work also for mutual transits.

We recall briefly the method that relies on Green's theorem converting an integral over a surface into an integral over the contour of that surface:

$$\iint_{\mathcal{S}} \omega(x,y)\, dx\, dy = \oint_{\partial\mathcal{S}} \left(f_x(x,y)\, dx + f_y(x,y)\, dy\right). \tag{50}$$

In this equation, $\partial\mathcal{S}$ is the boundary of $\mathcal{S}$, and $\omega(x,y)$ the exterior derivative of $\mathbf{f}(x,y) = (f_x, f_y)$ defined by

$$\omega(x,y) = \frac{\partial f_y}{\partial x} - \frac{\partial f_x}{\partial y}. \tag{51}$$

When the planet is crossing the limb of the star, the boundary is the union of two circular arcs. One of them follows the edge of the planet centered on (x_0, y_0) with radius r. The coordinates of any points of this arc and the tangent vectors are of the form

$$x = x_0 + r\cos\varphi\,, \qquad dx = -r\sin\varphi\,d\varphi\,,$$
$$y = y_0 + r\sin\varphi\,, \qquad dy = r\cos\varphi\,d\varphi\,. \tag{52}$$

The angle φ varies between two limits $\varphi_p^{(1)}$ and $\varphi_p^{(2)}$, corresponding to the intersections A and B between the circumferences of the planet and of the star, respectively (see Fig. 2). The second arc fellows the edge of the star and is parameterized by the coordinates

$$x = \cos\varphi\,, \qquad dx = -\sin\varphi\,d\varphi\,,$$
$$y = \sin\varphi\,, \qquad dy = \cos\varphi\,d\varphi\,, \tag{53}$$

with φ going from $\varphi_s^{(1)}$ to $\varphi_s^{(2)}$ associated to the intersections B and A, respectively.

More generally, if we denote $(x_j, y_j)_{j=p,s}$ as the centers of the arcs, and $(r_j)_{j=p,s}$ as their radii such that

$$x(\varphi) = x_j + r_j\cos\varphi\,, \qquad \text{and} \qquad y(\varphi) = y_j + r_j\sin\varphi\,, \tag{54}$$

we obtain (Pál 2012)

$$\iint_{\mathcal{S}_p} \omega(x,y)\,dx\,dy =$$
$$\sum_{j=p,s} \int_{\varphi_j^{(1)}}^{\varphi_j^{(2)}} \left(f_y(x(\varphi),y(\varphi))\cos\varphi - f_x(x(\varphi),y(\varphi))\sin\varphi \right) r_j\,d\varphi\,. \tag{55}$$

Here, we are interesting in the cases where $\omega(x,y)$ stands for 1, x, y, x^2, y^2, or xy. The field vectors $\mathbf{f}(x,y)$ associated to those $\omega(x,y)$ are not uniquely determined. We choose $(-\frac{1}{2}y, \frac{1}{2}x)$, $(-xy, 0)$, $(0, xy)$, $(-x^2y, 0)$, $(0, xy^2)$, and $(-\frac{1}{4}xy^2, \frac{1}{4}x^2y)$, respectively. We denote $\omega_{ij} = x^iy^j$ and $\mathbf{f}_{ij}(x,y)$ as the functions whose exterior derivative is ω_{ij}. The integral of $\mathbf{f}_{ij}$ along a circular arc reads as

$$F_{ij}(\varphi) = \int \big(f_{ij,y}(x_0 + r\cos\varphi, y_0 + r\sin\varphi)\cos\varphi$$
$$- f_{ij,x}(x_0 + r\cos\varphi, y_0 + r\sin\varphi)\sin\varphi \big) r\,d\varphi\,. \tag{56}$$

Since the $\mathbf{f}_{ij}$ are polynomials in x and y, the F_{ij} can be computed using the recurrence relations provided by Pál (2012). The results are displayed in Table 2 for $i = 0, 1, 2$, and $j = 0, 1, 2$. From them, one can derive the quantities present in the expressions of the flux fraction f, the subplanet velocity v_p and the width β_p:

$$\mathcal{S}_p = \langle 1 \rangle = \iint \omega_{00}\,,$$
$$\bar{x} = \langle x \rangle = \frac{1}{\mathcal{S}_p} \iint \omega_{10}\,,$$
$$\bar{y} = \langle y \rangle = \frac{1}{\mathcal{S}_p} \iint \omega_{01}\,,$$
$$\left\langle (x - \bar{x})^2 \right\rangle = \left(\frac{1}{\mathcal{S}_p} \iint \omega_{20} \right) - \bar{x}^2\,, \tag{57}$$
$$\left\langle (y - \bar{y})^2 \right\rangle = \left(\frac{1}{\mathcal{S}_p} \iint \omega_{02} \right) - \bar{y}^2\,,$$
$$\left\langle (x - \bar{x})(y - \bar{y}) \right\rangle = \left(\frac{1}{\mathcal{S}_p} \iint \omega_{11} \right) - \bar{x}\bar{y}\,.$$
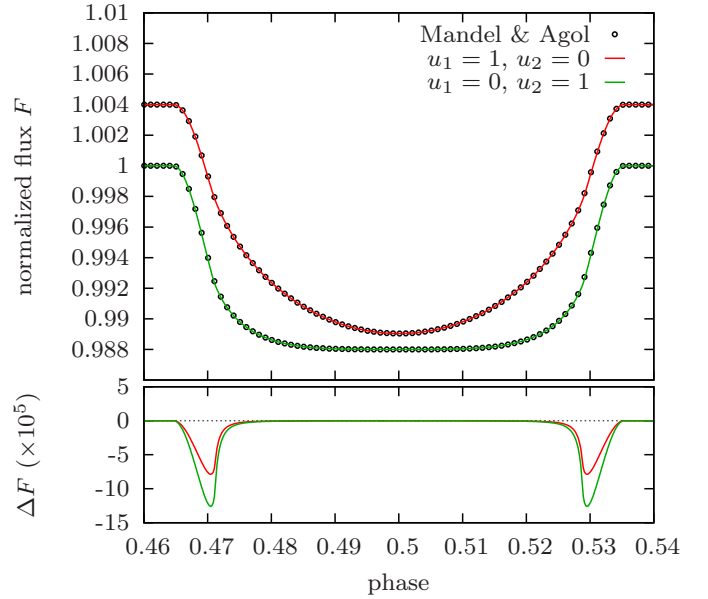
Fig. 3. Transit light curves for $r = 0.1$ and quadratic limb-darkening with two sets of coefficients u_1, u_2. The solid curves in red and in green are obtained from the approximation (35), while the black open circles are computed using the routine of Mandel & Agol (2002).

5. Comparison with simulations

5.1. Transit light curve

Although it was not the main goal of this present work, in the derivation of a precise modeling of the RM effect, we obtained a new expression of the flux fraction f occulted by a planet during a transit (see Eq. (35)). In comparison to existing formulas that are exact (e.g. Mandel & Agol 2002; Pál 2012), the one of this paper relies on an expansion of the intensity in the vicinity of the averaged position of the planet. We thus expect our formulation to be less precise.

Figure 3 shows the comparison between the approximation (35) and the exact formula derived by Mandel & Agol (2002). By eye, it is not possible to distinguish between the two approaches. In the residuals, however, we can see that the maximum of deviation occurs close to the limb, more exactly, when the edge of the planet is tangent to that of the star. Indeed, at the border of the star, the limb-darkening becomes steeper and steeper, and the derivatives $\partial_x I_\alpha(x, y)$ and $\partial_y I_\alpha(x, y)$ even go to infinity for $\alpha < 2$. Nevertheless, this singularity is smoothed out by the decrease in the overlapping area between the planet and the star disks during ingress and egress.

One advantage of the present formula is that it can be easily generalized to more complex problems, as in the cases of a distorted planet, distorted star, important gravity limb-darkening, and so on. For our purpose, it provides an accurate enough estimation of the flux that can be used to derive the RM effect.

5.2. Subplanet profile

We checked the accuracy of our new formulas of the subplanet velocity v_p (37) and the width $\beta_p^2 = \beta_0^2 + \delta\beta_p^2$ with $\delta\beta_p$ given by (40). For that, we used the software called SOAP, for Spot Oscillation And Planet (Boisse et al. 2012), to produce artificial data as close as possible to real observations. This code is a numerical tool that models radial velocity and photometry observations

Table 2. Integrals F_{ij} (56) of the field vectors $\mathbf{f}_{ij}(x, y)$ along a circular arc centered on (x_0, y_0) with radius r.

$$F_{0,0}(\varphi) = \frac{1}{2}r(r\varphi + x_0 \sin\varphi - y_0 \cos\varphi)$$

$$F_{1,0}(\varphi) = -x_0 y_0 r \cos\varphi - \frac{1}{2}y_0 r^2 \cos^2\varphi + \frac{1}{4}x_0 r^2(2\varphi - \sin 2\varphi) + \frac{1}{12}r^3(3\sin\varphi - \sin 3\varphi)$$

$$F_{0,1}(\varphi) = x_0 y_0 r \sin\varphi + \frac{1}{2}x_0 r^2 \sin^2\varphi + \frac{1}{4}y_0 r^2(2\varphi + \sin 2\varphi) - \frac{1}{12}r^3(3\cos\varphi + \cos 3\varphi)$$

$$F_{2,0}(\varphi) = -x_0^2 y_0 r \cos\varphi - x_0 y_0 r^2 \cos^2\varphi + \frac{1}{4}x_0^2 r^2(2\varphi - \sin 2\varphi) - \frac{1}{12}y_0 r^3(3\cos\varphi + \cos 3\varphi) + \frac{1}{6}x_0 r^3(3\sin\varphi - \sin 3\varphi) + \frac{1}{32}r^4(4\varphi - \sin 4\varphi)$$

$$F_{0,2}(\varphi) = x_0 y_0^2 r \sin\varphi + x_0 y_0 r^2 \sin^2\varphi + \frac{1}{4}y_0^2 r^2(2\varphi + \sin 2\varphi) + \frac{1}{12}x_0 r^3(3\sin\varphi - \sin 3\varphi) - \frac{1}{6}y_0 r^3(3\cos\varphi + \cos 3\varphi) + \frac{1}{32}r^4(4\varphi - \sin 4\varphi)$$

$$F_{1,1}(\varphi) = \frac{1}{4}x_0 y_0 r(2r\varphi + x_0 \sin\varphi - y_0 \cos\varphi) + \frac{1}{8}x_0^2 r^2 \sin^2\varphi - \frac{1}{8}(y_0^2 + r^2)r^2 \cos^2\varphi + \frac{1}{48}y_0 r^3(15\sin\varphi - \sin 3\varphi) - \frac{1}{48}x_0 r^3(15\cos\varphi + \cos 3\varphi)$$

of stars with spots. It has been updated recently to also model the effect of a planet transiting a spotted star, and was renamed SOAP-T (Oshagh et al. 2012). Briefly, the code divides the disk of the star into a grid. To each cell of that grid, a Gaussian profile with a width β_0 and amplitude $I(x, y)$ (in our notation) is assigned. This represents the intrinsic line profile of the nonrotating star as detected by the instrument. These lines are then shifted in velocity according to their position with respect to the spin-axis and the $V \sin i_\star$ of the star. All the lines of the cells uncovered by any spots or planets are added together to produce an artificial CCF that is then fitted by a Gaussian to derive a radial velocity.

With SOAP-T, we produced the CCF of a star with a transiting planet at different positions of the planet on the disk. We also generated the CCF of the same star while the planet is not transiting, and by taking the difference, we got the subplanet profile. Such profiles are displayed in Fig. 4 for different values of $V \sin i_\star$. Unless specified explicitly, here, and in all the following simulations, the star is a solar-type star with a quadratic limb-darkening law whose coefficients are $u_1 = 0.38$, $u_2 = 0.3$, and an intrinsic line width without rotation of $\beta_0 = 3$ km.s^{-1}. The planet is a Jupiter evolving in the equatorial plane of its star, its radius is $r = R_p/R_{star} = 0.1099$. In Fig. 4, the subplanet line profiles of low rotating stars are Gaussian. This results from the hypothesis of SOAP-T, which assumes Gaussian intrinsic line profiles. But we observe that the Gaussian shape holds even for $V \sin i_\star = 20$ km.s^{-1}, which validates our assumption leading to Eq. (14).

To each of the artificial subplanet profiles generated with SOAP-T, we also computed the mean velocity v_p and the dispersion β_p, to be compared with our formulas (37) and (40). Figure 5 shows the results for v_p after normalization to remove the effect of the $V \sin i_\star$ of the star. We checked that the figure is indeed unchanged up to $V \sin i_\star = 20$ km.s^{-1}. The numerical outputs obtained with SOAP-T are plotted against two different analytical approximations denoted S_0 and S_2. In S_0, the surface brightness of the star is taken uniform below the disk of the planet, while in S_2, the second derivatives are taken into account as in (37). We observe that where the error is maximal, close to the limb, S_2 improves the determination of v_p by about a factor 3 with respect to S_0. In the case $r = 0.1$ and $V \sin i_\star = 10$
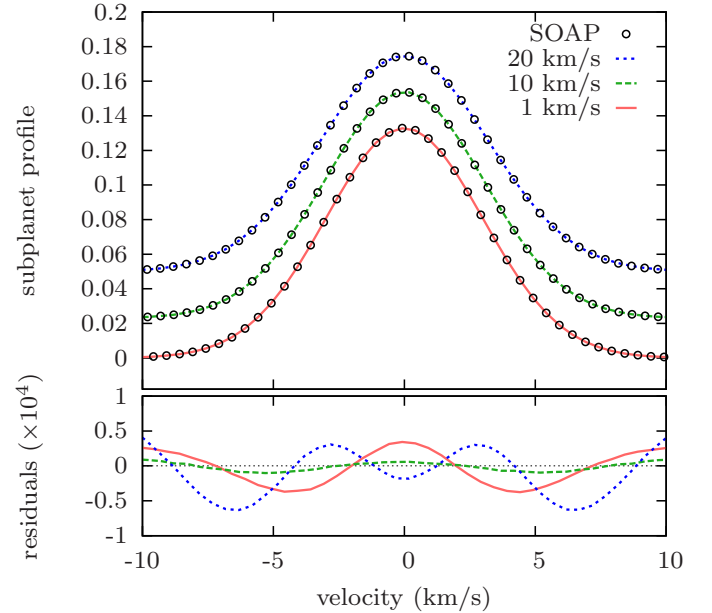
Fig. 4. Example of subplanet line profiles obtained with SOAP-T (circles), compared with Gaussian profiles (curves) for different stellar $V \sin i_\star$.

km.s^{-1}, the maximal error provided by S_2 is about 20 m/s which represents a relative difference of 0.2%.

In the case of the dispersion β_p, the difference between the estimation derived assuming uniform (S_0) and nonuniform (S_2) brightness below the planet disk is more evident (see Fig. 6). Indeed, in the former case, β_p remains constant and equal to the width β_0 of the nonrotating star line profile, while we observe that for the simulated and the modeled line profiles, the shape of β_p as a function of the orbital phase looks like a trapezoid with the large base at β_0 and the maximum at approximately
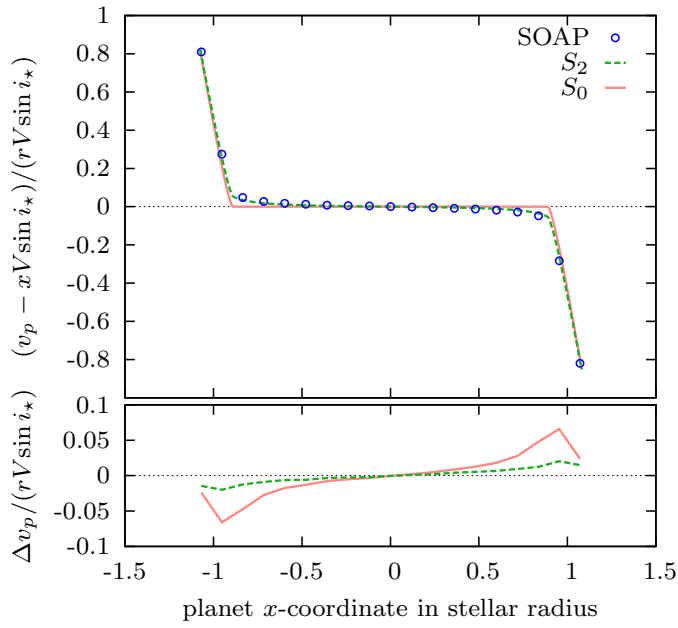
$$\sqrt{\beta_0^2 + (r V \sin i_\star)^2/4}.$$

Fig. 5. Subplanet velocity v_p produced with SOAP-T (blue points), approximation S_0 assuming uniform intensity below the disk of the planet (red curve), and approximation S_2 taking the second derivatives of the stellar surface brightness into account, Eq. (37) (green curve).
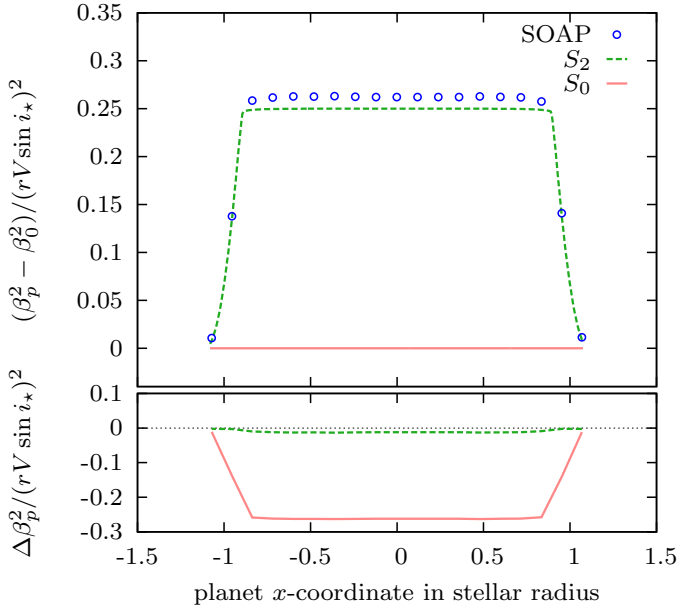

Fig. 6. Subplanet dispersion β_p produced with SOAP-T (blue points), approximation S_0 (red curve), and approximation S_2, Eq. (40), (green curve).

5.3. Rossiter-McLaughlin effect

We now compare our analytical expression of the Rossiter-McLaughlin effect v_{CCF} (14) with signals generated with SOAP-T, which simulates the reduction analysis of the CCF technique numerically.

Figure 7 displays the results for different $V \sin i_\star$. As long as $V \sin i_\star$ is below or equal to 10 km.s^{-1}, the error induced by the analytical formula remains lower than ~1 m/s, which is close

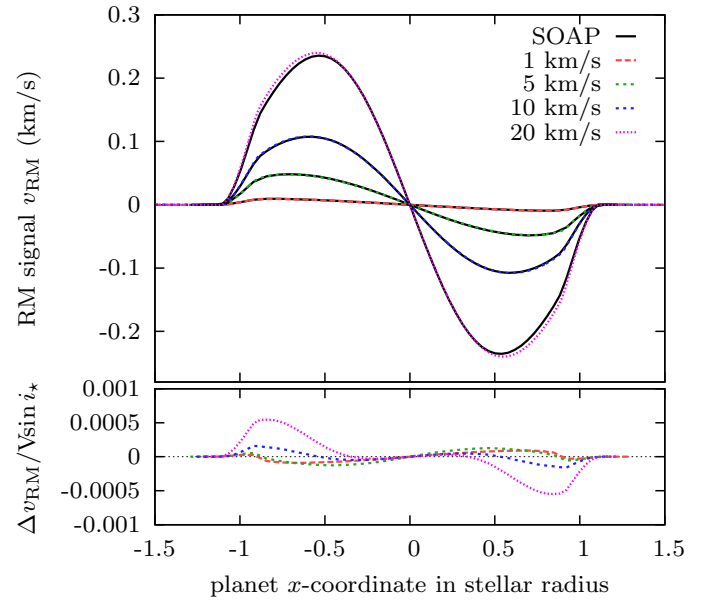**Fig. 7.** RM signals produced with SOAP-T (solid black curves) for different $V \sin i_\star$, and results of v_{CCF} (14) (different dashed curves).

to the magnitude of the precision of RV measurements. In that case, the analytical approximations are almost indistinguishable from the numerical simulations. However, for larger $V \sin i_\star$, the agreement between numerical signals and analytical ones is weaker. For example, when $V \sin i_\star = 20$ km.s^{-1}, the analytical approximation leads to a maximal error of 10 m/s, which is 5% of the amplitude of the signal. Nevertheless, it should also be noted that for fast-rotating stars the spreading of the spectral lines over the detectors decreases the precision of the measurements. In any case, the analytical expression v_{CCF} brings a definite improvement over other formulas, which have not been designed to simulate the CCF technique as we see in the following section.

5.4. Comparison between different techniques

To highlight the effect of the instrument and of the data reduction analysis, we generated different models of line profile and compared the RM signals computed numerically with the results of the analytical formulas v_{CCF} (14) and v_{iodine} (27). In our examples, the line profiles are of three types: $\mathcal{F}_{\text{HIRES}}(v)$, $\mathcal{F}_{\text{HARPS}}(v)$, and $\mathcal{F}_{\text{CORALIE}}(v)$. They are associated to three RM signals: v_{HIRES}, v_{HARPS}, and v_{CORALIE}, respectively. It should be stressed that the goal is not to reproduce the lines observed by those instruments exactly, but to capture their main characteristics. On the one hand, HIRES and HARPS are two spectrographs with high resolutions that we assume to be identical with a width $\beta_0 = 2.6$ km.s^{-1} for nonrotating solar-type stars. On the other hand, the resolution of CORALIE is about twice lower, and the intrinsic width of the same stars is about $\beta_0 = 4.5$ km.s^{-1} (Santos et al. 2002). We consider a star with $V \sin i_\star = 15$ km.s^{-1}, which is adapted to our illustration. Finally, the transiting planet is a Jupiter-like planet with a radius $R_p = 0.1 R_{\text{star}}$.

Figure 8 shows the simulated line profiles. The panel 8a displays the rotation kernel $\mathcal{R}(v)$, a stellar profile $\mathcal{F}_{\text{star}}(v)$ with $\beta_0 = 2.6$ km.s^{-1}, and a subplanet profile $\mathcal{F}_{\text{pla}}(v - v_p)$ multiplied by the flux fraction f, and computed with $\beta_p = (\beta_0^2 + (rV \sin i_\star/4)^2)^{1/2}$. Figure 8b depicts the resulting line profiles
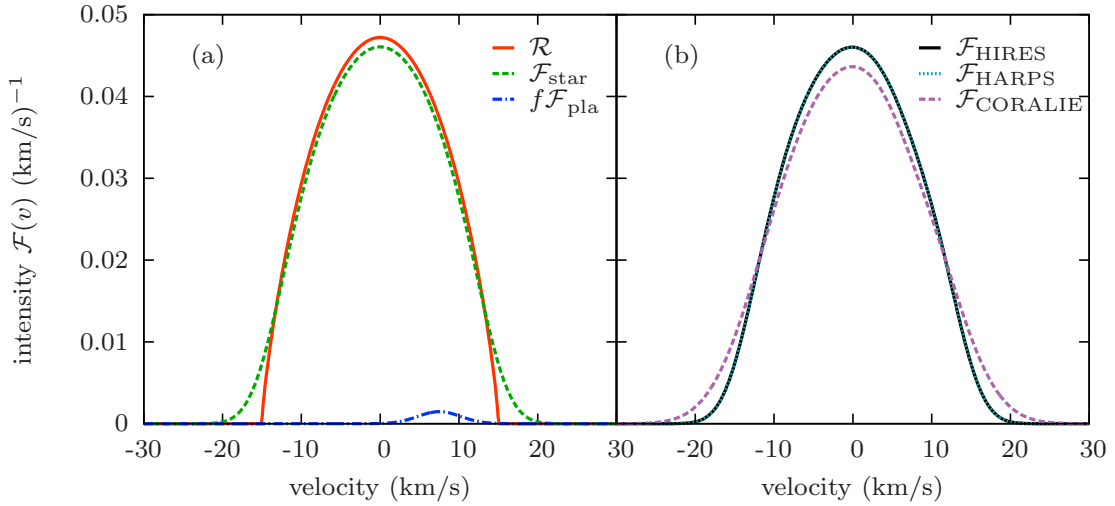
Fig. 8. Simple models of line profiles. (a) Rotation kernel $\mathcal{R}(v)$ with $V\sin i_\star = 15$ km.s^{-1} in solid red, stellar line profile assuming $\beta_0 = 2.6$ km.s^{-1} in dashed green, subplanet line profile $\mathcal{F}_{\text{pla}}(v)$ with $\beta_p = 2.71$ km.s^{-1} in dash-dotted blue. (b) $\mathcal{F}_{\text{transit}} = \mathcal{F}_{\text{star}} - f\mathcal{F}_{\text{pla}}$ modeling an average line profile observed with HIRES in solid black, and a CCF observed with HARPS in dotted cyan. The same with $\beta_0 = 4.5$ km.s^{-1} and $\beta_p = 4.56$ km.s^{-1} represents a CCF observed by CORALIE, in dashed violet.

during transit $\mathcal{F}_{\text{HIRES}}(v)$, $\mathcal{F}_{\text{HARPS}}(v)$, and $\mathcal{F}_{\text{CORALIE}}(v)$. Following our hypothesis, $\mathcal{F}_{\text{HIRES}}(v)$ is identical to $\mathcal{F}_{\text{HARPS}}(v)$.

From the simulated line profiles, we derived RM signals numerically. The signal v_{HIRES} was obtained from $\mathcal{F}_{HIRES}$ using the iodine cell technique, i.e., by fitting the best Doppler shift between a line without transit deformation, and the line profiles computed during transit. Both v_{HARPS}, and v_{CORALIE} are the results of applying the CCF technique, i.e., a numerical fit between a shifted Gaussian and $\mathcal{F}_{\text{HARPS}}$ and $\mathcal{F}_{\text{CORALIE}}$, respectively. We also generated $v_{C\text{max}}$ by maximizing the cross-correlation $C(\bar{v})$ between the line profiles $\mathcal{F}_{\text{HIRES}}$ at and out of transit. These four RM signals are represented in Fig. 9a. It is notable that the RM effects associated to the three instruments are all different. The variation between v_{HARPS} and v_{CORALIE} is only due to the change in resolution. However, in the case of v_{HIRES} and v_{HARPS}, the simulated lines are exactly identical. The observed difference in the RM signal is the result of the chosen data reduction technique. Figure 9a also confirms that the maximum of the cross-correlation $C(\bar{v})$ gives the same result as the iodine cell technique (when the stellar lines are symmetrical) since $v_{\text{HIRES}} = v_{C\text{max}}$.

The last three panels of Fig. 9 represent the comparison between the simulated RM signals and the analytical formulas v_{CCF} (14), and v_{iodine} (27) associated to the CCF and the iodine cell technique, respectively. We observe that the formulas adapted to the analysis routines are in good agreement with the respective simulations. We also notice that for CORALIE, whose resolution is lower, the two analytical formulas give roughly the same result. This is because the stellar line is less affected by the rotational kernel and is more Gaussian. We show that, in that case, the two methods should indeed provide the same result (see Sect. 2.3).

From this study, we conclude that a given star observed by two different techniques should present two distinct RM signals. To date, this notable result has not been seen since the instruments with the highest signal-to-noise, HIRES and HARPS, are located in two different hemispheres. This makes it difficult to observe the same stars. For those observed with other instruments, the expected gaps are diluted by the measurement uncertainties. Nevertheless, with the advent of HARPS-North, we may observe such discrepancies in the future.

5.5. Biases on fitted parameters

As a final test, we simulated artificial data from either the CCF or the iodine cell model, and we fit each of these data with the two models separately. The goal is not to perform an exhaustive study of the biases introduced by the application of a wrong model in the process of fitting data, but to give an example with some typical parameters.

For this illustration, we considered only one set of parameters. As in the previous section, the star has $V\sin i_\star = 15$ km.s^{-1} with intrinsic line width $\beta_0 = 2.6$ km.s^{-1}. We chose a quadratic limb-darkening characterized by $u_1 = 0.69$ and $u_2 = 0.0$. The planet's radius is taken equal to $R_p = 0.1R_{\text{star}}$. The impact parameter of the orbit is assumed to be $0.3R_{\text{star}}$. For information, this value is that of a planet with a semi-major axis $a = 4R_{\text{star}}$ and an inclination $i = 85.7$ deg. All these parameters were fixed throughout all the simulations. Only the projected spin-orbit angle λ_{input} was varied from 0 to 90 degrees by steps of ten degrees. For each value of λ_{input}, and each model, 1 000 datasets were generated with a Gaussian noise of 10 m/s. Each simulation contains 50 points, among which 32 are inside the transit and 18 outside. In each case, we fit both the $V\sin i_\star$ and the projected spin-orbit angle.

Figure 10 shows the results of this analysis in the case where the data are generated with the CCF model v_{CCF} (Eq. (14)). As expected, the parameters recovered with the appropriate model are accurate, while those deduced from the iodine cell technique formulas are biased. The bias on $V\sin i_\star$ is systematically positive and also the most important, especially at large projected spin-orbit angle ($\lambda_{\text{input}} \approx 90$ deg) where we get $(V\sin i_\star)_{\text{fit}} = 20.7 \pm 0.5$ km.s^{-1} instead of 15 km.s^{-1}. One can notice that this agrees with the results of, e.g., Simpson et al. (2010) who applied the model of Hirano et al. on WASP-3 observed with SOPHIE. They fit a $V\sin i_\star = 15.7^{+1.4}_{-1.3}$ km.s^{-1} while the spectroscopic value is only 13.4 ± 1.5 km.s^{-1}. On the other hand, the
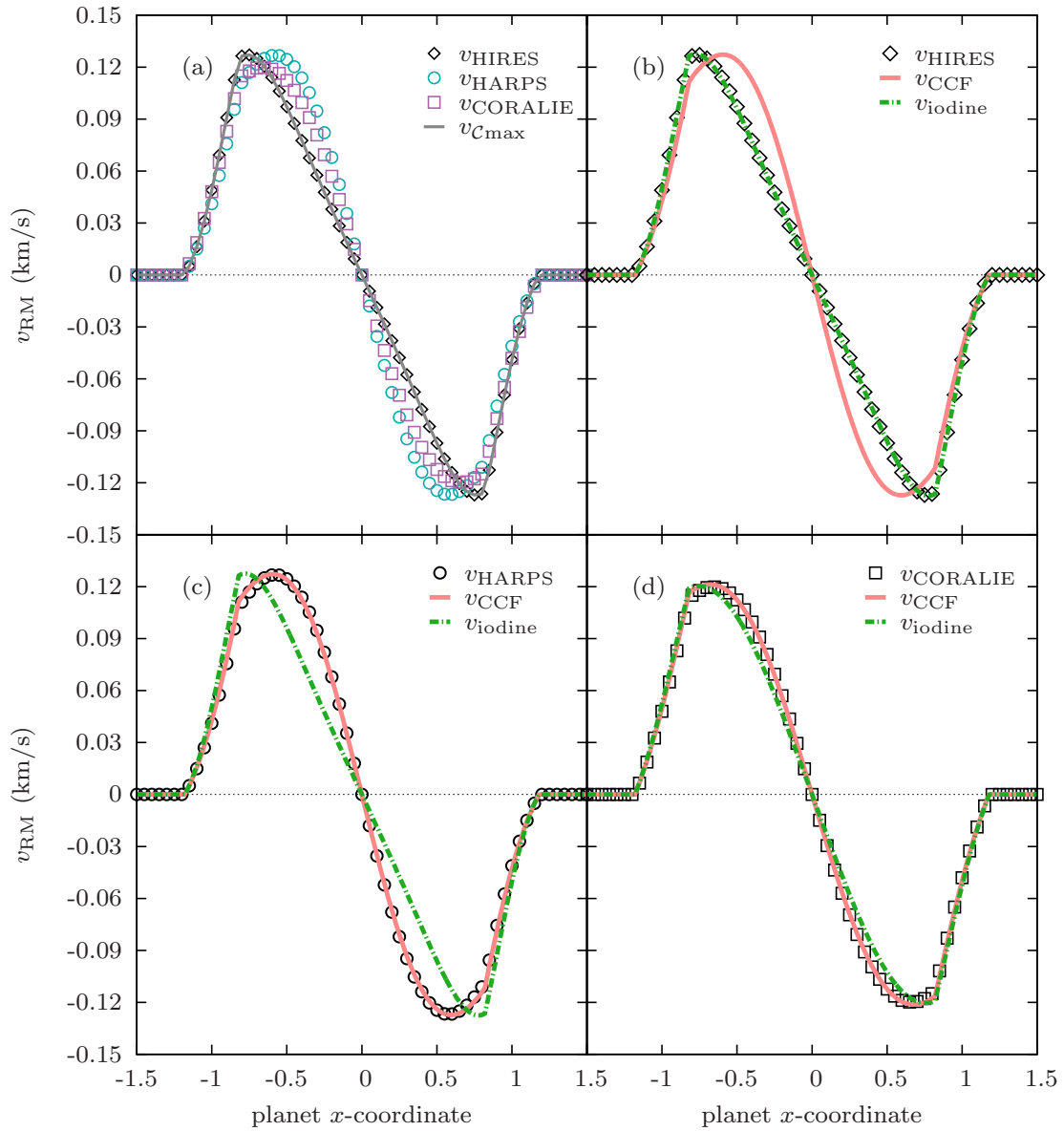
Fig. 9. Comparison of a simulated RM signal observed by different techniques and/or instruments. We used the line profiles of Fig. 8b. The open diamonds, circles and squares represent the RM signal obtained numerically with the iodine cell technique on the HIRES line profile, and with the Gaussian fit to the HARPS, or CORALIE, CCFs, respectively. In (a) The gray curve corresponds to the numerical maximization of the cross-correlation $C(\bar{v})$ of the HIRES profiles inside and outside transits. In (b), (c), and (d), the numerical RM signal computed on the HIRES, HARPS, and CORALIE line profiles, respectively, are compared with the analytical formulas v_{CCF} (14) in solid red and v_{iodine} (27) in dash-dotted green.

bias on the fitted projected spin-orbit angle λ_{fit} remains within 2-σ. This parameter is thus less affected by the model.

The difference in behavior between $(V \sin i_\star)_{fit}$ and λ_{fit} is more evident in Fig. 11. In that case, the data were simulated with the formulas associated to the iodine cell technique: v_{iodine} (Eq. (27)). As in the previous test, using the same model for both the generation of the data and the fit, leads to very accurate estimations of the parameters, while the application of the wrong model introduces biases. The $(V \sin i_\star)_{fit}$ is systematically negative as we could expect since the situation is the opposite of the one in the previous paragraph. Nevertheless, the error is smaller. In the worst case, we get $(V \sin i_\star)_{fit} = 11.9 \pm 0.3$ km.s^{-1}, which represents on error of the order of 3 km.s^{-1}, while it was almost 6 km.s^{-1} in the previous example. The situation is similar for

λ_{fit}. We observe small biases anticorrelated with those of the previous test, but now, the inaccuracy remains within 1-σ.

We stress that we only fit two parameters in this study, while the others are fixed to their exact values. We already observe that the best fits tend to compensate for inaccurate models by introducing biases. With more free parameters, there are more possibilities to balance the model, and it is thus difficult to predict the behavior of the fit. Since the models are not linear, we should expect the presence of several local minima. Eventually, in some of them, the projected spin-orbit angle might be more biased than in our tests. This should be analyzed on individual case bases, which is not the goal of this paper.
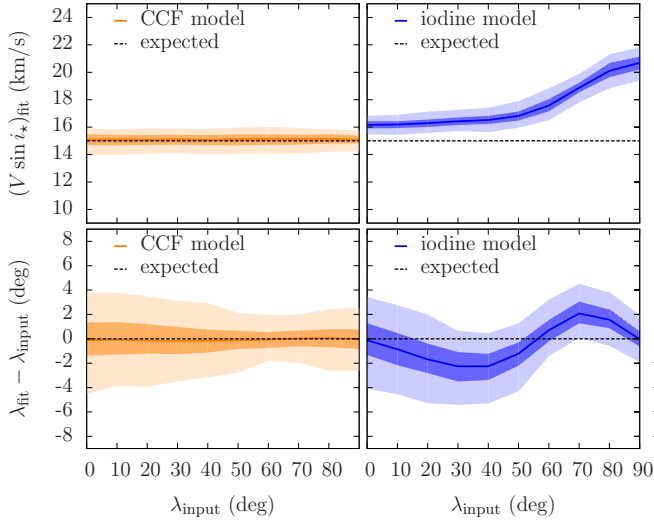
Fig. 10. Results of the fits with two different models of mock data generated by the CCF technique formulas. In each panel, the area with the lightest color represents the two-sigma limit, the darkest color is the one-sigma threshold, and the curve is the best value.
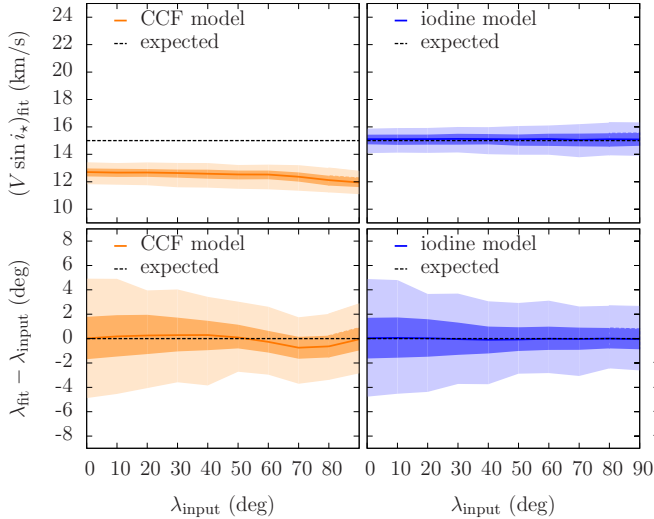

Fig. 11. Same as Fig. 10 but for data simulated with the iodine cell technique formulas.

6. Conclusion

One of the main objectives of this paper has been to highlight that there is no unique way of measuring RM effects and that different techniques provide different values of RV anomalies. RM signals should thus be analyzed using the appropriate model to avoid any biases, at least in $V \sin i_\star$. This is particularly important in the case of low-impact parameters (planet passing close to the center of its star) since then, the projected spin-orbit angle only depends on the amplitude of the RM signal.

We provided a new analytical formula specially designed to model RV anomalies obtained by fitting a Gaussian function to the CCF, as in the analysis routines of HARPS and SOPHIE. We also revisited the modeling of the iodine cell technique, as used with HDS and HIRES, for which we derived an analytical expression adapted to non-Gaussian stellar line profiles. An effort was made to model the effect of the rotation of the star on the

width of the subplanet line profile. Since our formulas do not rely on any expansion in powers of the subplanet velocity v_p, our results remain stable even for fast-rotating stars.

The advantage of having a purely analytical expression to model the RM effect is the rapidity of computation. It can thus be used to analyze a large sample of RM signals uniformly. As a complement to this paper, we make our code accessible to the community as a free open source software package. This is a library called ARoME, an acronym for Analytical Rossiter-McLaughlin Effect, designed to generate analytical RM signals based on the formulas of the paper. It also includes the effect of macro-turbulence as described in the Appendix A. The library provides a C interface and, optionally, a Fortran 77 or 2003 interface to be called by an application. The fully documented package can be downloaded from the webpage www.astro.up.pt/resources/arome.

Besides the modeling of the RM effect, we also analytically derived a new expression for transit light curves (35). Although this expression is the result of a Taylor expansion of the intensity and is only adapted to small planets, it gives good approximations. Moreover, the expression is general enough to be easily extended to more complex problems.

Appendix A: Macro-turbulence

Here, we study the effect of macro-turbulence on the Rossiter-McLaughlin signal. We consider only the "radial-tangential" model as in (Hirano et al. 2011). In that case, if we denote $\mathcal{F}_0(v)$ as the line profile of the nonrotating star without macro-turbulence, the subplanet line profile reads as

$$\mathcal{F}_{\text{pla}}(v) = [\mathcal{F}_0 * M](v) , \tag{A.1}$$

where $M(v)$ is the rotation-turbulence kernel given by (Gray 2005),

$$M(v) = \iint_{\mathcal{S}_p} I(x, y) \Theta(x, y, v - x V \sin i_\star) \, dx \, dy , \tag{A.2}$$

and

$$\Theta(x, y, v) = \frac{1}{2} (\Theta_R(x, y, v) + \Theta_T(x, y, v))$$
$$= \frac{1}{2\sqrt{\pi}} \left(\frac{1}{\zeta \cos\theta} e^{-\left(\frac{v}{\zeta\cos\theta}\right)^2} + \frac{1}{\zeta \sin\theta} e^{-\left(\frac{v}{\zeta\sin\theta}\right)^2} \right) . \tag{A.3}$$

We highlight the different dependencies on (x, y), on the one hand, through $\cos\theta = \sqrt{1 - x^2 - y^2}$ and $\sin\theta = \sqrt{x^2 + y^2}$, and on the velocity v, on the other. The coordinates (x, y) are normalized by the radius of the star. Since Θ is the sum of two

Gaussians Θ_R and Θ_T associated to the radial and the tangential broadenings, respectively, we also split $M(v)$ into two parts

$$M(v) = \frac{1}{2}(M_R(v) + M_T(v)) , \tag{A.4}$$

such that $M_R(v)$ is associated to Θ_R, and $M_T(v)$ is associated to Θ_T.

Now, we compute the moments of $(M_j(v))_{j=R,T}$ as in Sect. 4 to evaluate the effect of the rotation-turbulence kernel on the subplanet profile. We have

$$\langle v^n \rangle_{M_j} = \frac{1}{A_j} \int_{-\infty}^{+\infty} dv\, v^n$$
$$\times \iint_{\mathcal{S}_p} dx\, dy\, I(x,y)\Theta_j(x,y,v - xV\sin i_\star) , \tag{A.5}$$

where A_j is a normalization constant whose expression is

$$A_j = \int_{-\infty}^{+\infty} dv \iint_{\mathcal{S}_p} dx\, dy\, I(x,y)\Theta_j(x,y,v - xV\sin i_\star) . \tag{A.6}$$

Inverting the integrals, we get, for the normalization,

$$A_j = \iint_{\mathcal{S}_p} dx\, dy\, I(x,y) \int_{-\infty}^{+\infty} dv\, \Theta_j(x,y,v - xV\sin i_\star) . \tag{A.7}$$

Since $\Theta_j(x,y,v)$ (A.3) is normalized, the inner integral on the velocity is one. It thus remains only

$$A_R = A_T = A = \iint_{\mathcal{S}_p} I(x,y)\, dx\, dy , \tag{A.8}$$

as in Sect. 4. We now focus on the numerator of (A.5). By construction, $\langle v^0 \rangle_{M_j} = 1$. Then, using the inversion of integrals, we get

$$v_p^{(j)} := \langle v \rangle_{M_j} = \frac{1}{A} \iint_{\mathcal{S}_p} dx\, dy \left[I(x,y) \right.$$
$$\left. \times \int_{-\infty}^{+\infty} dv\, v\, \Theta_j(x,y,v - xV\sin i_\star) \right]. \tag{A.9}$$

The inner integral over the velocity v gives $xV\sin i_\star$, we have thus

$$v_p^{(j)} = V\sin i_\star \frac{\iint_{\mathcal{S}_p} x I(x,y)\, dx\, dy}{\iint_{\mathcal{S}_p} I(x,y)\, dx\, dy} \tag{A.10}$$

for each broadening: radial ($j = R$) and tangential ($j = T$). This is identical to (36). Finally, the second moment reads as

$$\mathcal{V}_2^{(j)} := \langle v^2 \rangle_{M_j} = \frac{1}{A} \iint_{\mathcal{S}_p} dx\, dy \left[I(x,y) \right.$$
$$\left. \times \int_{-\infty}^{+\infty} dv\, v^2\, \Theta_j(x,y,v - xV\sin i_\star) \right]. \tag{A.11}$$

The inner integral gives

$$\int_{-\infty}^{+\infty} dv\, v^2 \Theta_R(v - xV\sin i_\star) = \zeta^2 \cos^2\theta + x^2(V\sin i_\star)^2 \tag{A.12}$$

for the radial broadening, and

$$\int_{-\infty}^{+\infty} dv\, v^2 \Theta_T(v - xV\sin i_\star) = \zeta^2 \sin^2\theta + x^2(V\sin i_\star)^2 \tag{A.13}$$

for the tangential broadening. We thus have

$$\mathcal{V}_2^{(R)} = \zeta_R^2 + \mathcal{V}_2 \quad \text{and} \quad \mathcal{V}_2^{(T)} = \zeta_T^2 + \mathcal{V}_2 , \tag{A.14}$$

with

$$\zeta_R^2 = \zeta^2 \frac{\iint_{\mathcal{S}_p} \cos^2\theta\, I(x,y)\, dx\, dy}{\iint_{\mathcal{S}_p} I(x,y)\, dx\, dy} , \tag{A.15}$$

$$\zeta_T^2 = \zeta^2 \frac{\iint_{\mathcal{S}_p} \sin^2\theta\, I(x,y)\, dx\, dy}{\iint_{\mathcal{S}_p} I(x,y)\, dx\, dy} , \tag{A.16}$$

where $\mathcal{V}_2$ corresponds to the case without macro-turbulence (Eq. (39)). It should be noted that $\zeta_R^2 + \zeta_T^2 = \zeta^2$. Let β_0 be the dispersion of $\mathcal{F}_0(v)$, and $\delta\beta_p$ the dispersion due to the rotational broadening alone (40). The subplanet line profile $\mathcal{F}_{\text{pla}}$ (A.1) can be approximated by the sum of two Gaussian functions

$$\mathcal{F}_{\text{pla}}(v - v_p) = \frac{1}{2}(\mathcal{G}_{\beta_R}(v - v_p) + \mathcal{G}_{\beta_T}(v - v_p)) \tag{A.17}$$

centered on the same value v_p with respective dispersions

$$\beta_R^2 = \beta_0^2 + \delta\beta_p^2 + \zeta_R^2 , \tag{A.18}$$

and

$$\beta_T^2 = \beta_0^2 + \delta\beta_p^2 + \zeta_T^2 . \tag{A.19}$$

In this expressions, $\delta\beta_p$, ζ_R, and ζ_T are functions of the position of the planet on the stellar disk. With this model, the Rossiter-McLaughlin effect, as measured by the Gaussian fit of the CCF, reads as

$$v_{\text{CCF}} = -\frac{1}{2a_0} \left(\frac{2\sigma_0^2}{\sigma_0^2 + \beta_R^2} \right)^{3/2} f v_p \exp\left(-\frac{v_p^2}{2(\sigma_0^2 + \beta_R^2)} \right)$$
$$-\frac{1}{2a_0} \left(\frac{2\sigma_0^2}{\sigma_0^2 + \beta_T^2} \right)^{3/2} f v_p \exp\left(-\frac{v_p^2}{2(\sigma_0^2 + \beta_T^2)} \right) . \tag{A.20}$$

Appendix B: Normalization factor of the Gaussian fit

Appendix B.1: Without macro-turbulence

Here we detail the computation of the amplitude a_0 of the best Gaussian fit (13). In a first step we neglect the macro-turbulence and have

$$a_0 = 2\sigma_0 \sqrt{\pi} \left[\mathcal{G}_{\sigma_0} * \mathcal{F}_{\text{star}} \right](0) , \tag{B.1}$$

with $\mathcal{F}_{\text{star}} = \mathcal{F}_0 * \mathcal{R}$ and $\mathcal{R}$ is the normalized rotation kernel (B.14). If we assume that $\mathcal{F}_0$ is Gaussian with dispersion β_0, the associativity of the convolution product leads to

$$a_0 = 2\sigma_0 \sqrt{\pi} \left[\mathcal{G}_{\sigma_t} * \mathcal{R} \right](0)$$
$$= 2\sigma_0 \sqrt{\pi} \int_{-V\sin i_\star}^{V\sin i_\star} \mathcal{G}_{\sigma_t}(v)\mathcal{R}(v)\, dv , \tag{B.2}$$

with $\sigma_t^2 = \sigma_0^2 + \beta_0^2$. Finally, since $\mathcal{G}_{\sigma_t}(v)$ and $\mathcal{R}(v)$ are even functions of v, the expression of a_0 can be slightly simplified

$$a_0 = 4\sigma_0\sqrt{\pi}\int_0^{V\sin i_\star}\mathcal{G}_{\sigma_t}(v)\mathcal{R}(v)\,dv . \tag{B.3}$$

The amplitude a_0 is thus given by one single integral over a finite interval, which only has to be computed once. It can be done numerically using, for example, the simple trapezoidal rule explained in Press et al. (1992). In the case of quadratic limb-darkening, the result can also be expressed explicitly as a combination of modified Bessel functions and error functions (e.g. Hirano et al. 2010, Eq. F5).

Appendix B.2: With macro-turbulence

If the macro-turbulence is taken into account, it is not anymore possible to express the amplitude a_0 as a simple integral as in Sect. B.1. This is because the rotational-macroturbulence broadening kernel cannot be expressed as a convolution product (Gray 2005). But since a_0 brings only a small correction with respect to the Gaussian case (a_0 remains close to 1), we simplify the problem and approximate the line profile of the nonrotating star as a single Gaussian with dispersion β_0' given by

$$\beta_0'^2 = \beta_0^2 + \frac{\zeta^2}{2} \tag{B.4}$$

instead of two Gaussians with dispersion $\beta_{0,R}$ and $\beta_{0,T}$ defined by

$$\beta_{0,R}^2 = \beta_0^2 + \zeta^2\cos^2\theta \quad\text{and}\quad \beta_{0,T}^2 = \beta_0^2 + \zeta^2\sin^2\theta . \tag{B.5}$$

With this simplification, we recover the expression (B.3) where σ_t as to be replaced by σ_t' defined by $\sigma_t'^2 = \sigma_0^2 + \beta_0'^2$, i.e.,

$$a_0 = 4\sigma_0\sqrt{\pi}\int_0^{V\sin i_\star}\mathcal{G}_{\sigma_t'}(v)\mathcal{R}(v)\,dv . \tag{B.6}$$

Appendix B.3: Rotation kernel

We now give the expression of the rotation kernel $\mathcal{R}(v)$ present in the expression of the amplitude a_0 (B.3) and (B.6), without or with macro-turbulence, respectively. First, we consider a simpler kernel $\mathcal{R}_\alpha(v)$ associated to an intensity $I_\alpha(x,y)$ of the form

$$I_\alpha(x,y) = (1 - x^2 - y^2)^{\alpha/2} . \tag{B.7}$$

With $u = v/(V\sin i_\star)$, the rotation kernel (Gray 2005) reads as

$$\mathcal{R}_\alpha(v) = \frac{1}{V\sin i_\star}\int_{-\sqrt{1-u^2}}^{\sqrt{1-u^2}}(1 - u^2 - y^2)^{\alpha/2}\,dy . \tag{B.8}$$

To simplify the integral, we make the change of variable $z = y/\sqrt{1-u^2}$. We obtain

$$\mathcal{R}_\alpha(v) = \frac{b(\alpha)}{V\sin i_\star}\left(1 - \left(\frac{v}{V\sin i_\star}\right)^2\right)^{(\alpha+1)/2} , \tag{B.9}$$

where

$$b(\alpha) = \int_{-1}^1 (1 - z^2)^{\alpha/2}\,dz . \tag{B.10}$$

In practice, for the quadratic and the nonlinear limb-darkening, only the cases $\alpha = n/2$, $n \in \mathbb{N}$ are used. The integrals $b(\alpha)$ can thus be computed using the recurrence relation

$$b(\alpha) = \frac{\alpha}{\alpha+1}b(\alpha - 2) \tag{B.11}$$

with the initial conditions

$$\begin{aligned}
b(-1) &= \pi , \\
b(-1/2) &= \frac{\sqrt{\pi}\,\Gamma(3/4)}{\Gamma(5/4)} = 2.3962804694711844\ldots , \\
b(0) &= 2 , \\
b(1/2) &= \frac{\sqrt{\pi}\,\Gamma(1/4)}{\Gamma(3/4)} = 1.7480383695280799\ldots .
\end{aligned} \tag{B.12}$$

The normalized rotation kernel $\mathcal{R}(v)$ entering in the expression of the amplitude a_0 (B.3), or (B.6), which is associated to a normalized intensity

$$I(x,y) = \sum_n \gamma_n I_{\alpha_n}(x,y) \tag{B.13}$$

is then

$$R(v) = \sum_n \frac{\gamma_n b(\alpha_n)}{V\sin i_\star}\left(1 - \left(\frac{v}{V\sin i_\star}\right)^2\right)^{(\alpha_n+1)/2} . \tag{B.14}$$

Appendix C: RM signal measured by the iodine cell technique

In this section, we compute an analytical expansion of v_{iodine} (27) modeling the RM signal measured by the iodine cell technique. The expansion is made possible if the subplanet line profile $\mathcal{F}_{\text{pla}}$ and that of the nonrotating star $\mathcal{F}_0$ are both Gaussian. In that case, if we denote $\mathcal{G}_{\beta_0}(v) = \mathcal{F}_0$, $\mathcal{G}_{\beta_p}(v) = \mathcal{F}_{\text{pla}}(v)$, and $\mathcal{R}(v)$ as the rotation kernel, we have, on the one hand,

$$\frac{d\mathcal{F}_{\text{star}}(v)}{dv} = \left[\frac{d\mathcal{G}_{\beta_0}}{dv} * R\right](v) , \tag{C.1}$$

and, on the other hand,

$$\left[\frac{d\mathcal{F}_{\text{star}}}{dv} * \mathcal{F}_{\text{pla}}\right](v_p) = \left[\frac{d\mathcal{G}_{\beta_t}}{dv} * R\right](v_p) \tag{C.2}$$

with $\beta_t^2 = \beta_0^2 + \beta_p^2$. Thus, both the numerator and the denominator involve integrals of the form $(d\mathcal{G}_\sigma/dv) * R$. Let us consider the case where $\mathcal{R} = \mathcal{R}_\alpha$ with

$$\mathcal{R}_\alpha(v) = \frac{b(\alpha)}{V\sin i_\star}\left(1 - \left(\frac{v}{V\sin i_\star}\right)^2\right)^\eta \tag{C.3}$$

and $\eta = (\alpha + 1)/2$. The expansion in series of $(d\mathcal{G}_\sigma/dv) * \mathcal{R}_\alpha$ is obtained by expanding $\mathcal{R}_\alpha$ in the vicinity of $v = 0$. We have

$$\mathcal{R}_\alpha(v) = \frac{b(\alpha)}{V\sin i_\star}\sum_{k=0}^\infty \frac{(-\eta)_k}{k!}\left(\frac{v}{V\sin i_\star}\right)^{2k} , \tag{C.4}$$

where $(-\eta)_k = 1$ if $k = 0$, and $(-\eta)(-\eta + 1)\ldots(-\eta + k - 1)$ otherwise, is the Pochhammer symbol. It should be noted that if $\eta \in \mathbb{N}$, $(-\eta)_{\eta+1} = 0$, then the sum is finite and the expansion

exact. In the following, we consider only truncated sums up to an order K, i.e., $k \le K$. We then have

$$\left[\frac{d\mathcal{G}_\sigma}{dv} * \mathcal{R}_\alpha\right](\bar{v}) = \frac{1}{\sqrt{2\pi}\sigma}\frac{b(\alpha)}{V\sin i_\star}\sum_{k=0}^{K}\left(\frac{(-\eta)_k}{k!}\right.$$
$$\left.\times \int_{-V\sin i_\star}^{V\sin i_\star}\left(\frac{v}{V\sin i_\star}\right)^{2k}\frac{v-\bar{v}}{\sigma^2}\exp\left(-\frac{(v-\bar{v})^2}{2\sigma^2}\right)dv\right). \quad (C.5)$$

We apply the change of variable $x = (v - \bar{v})/\sigma$, and set $x_1 = -(V\sin i_\star + \bar{v})/\sigma$ and $x_2 = (V\sin i_\star - \bar{v})/\sigma$. We obtain

$$\left[\frac{d\mathcal{G}_\sigma}{dv} * \mathcal{R}_\alpha\right](\bar{v}) = \frac{1}{\sqrt{2\pi}\sigma}\frac{b(\alpha)}{V\sin i_\star}\sum_{k=0}^{K}\left(\frac{(-\eta)_k}{k!}\right.$$
$$\left.\times \int_{x_1}^{x_2}\left(\frac{x\sigma+\bar{v}}{V\sin i_\star}\right)^{2k}xe^{-x^2/2}\,dx\right). \quad (C.6)$$

The parenthesis inside the integral is then expanded which leads to

$$\left[\frac{d\mathcal{G}_\sigma}{dv} * \mathcal{R}_\alpha\right](\bar{v}) = \frac{1}{\sqrt{2\pi}\sigma}\frac{b(\alpha)}{V\sin i_\star}\sum_{k=0}^{K}\left(\frac{(-\eta)_k}{k!}\sum_{m=0}^{2k}\binom{2k}{m}\right.$$
$$\left.\times \left(\frac{\bar{v}}{V\sin i_\star}\right)^{2k-m}\left(\frac{\sigma}{V\sin i_\star}\right)^{m}\int_{x_1}^{x_2}x^{m+1}e^{-x^2/2}\,dx\right). \quad (C.7)$$

The expression is easier to handle when the two sums are inverted. For that, we introduce truncated hypergeometric functions of the form

$$F_K(a, b, c; x) = \sum_{k=0}^{K}\frac{(a)_k(b)_k}{(c)_k}\frac{x^k}{k!}, \quad (C.8)$$

and $Q_m(\eta; x)$ defined by

$$Q_{2p}(\eta; x) = \frac{(-\eta)_p}{p!}F_{K-p}\left(-\eta+p, p+\frac{1}{2}, \frac{1}{2}, x\right), \quad (C.9)$$

and

$$Q_{2p+1}(\eta; x) = 2x\frac{(-\eta)_{p+1}}{p!}$$
$$\times F_{K-p-1}\left(-\eta+p+1, p+\frac{3}{2}, \frac{3}{2}, x\right). \quad (C.10)$$

With these notations, we have

$$\left[\frac{d\mathcal{G}_\sigma}{dv} * \mathcal{R}_\alpha\right](\bar{v}) = \frac{1}{\sqrt{2\pi}\sigma}\frac{b(\alpha)}{V\sin i_\star}\sum_{m=0}^{2K}\left(Q_m\left(\eta; \frac{\bar{v}}{V\sin i_\star}\right)\right.$$
$$\left.\times \left(\frac{\sigma}{V\sin i_\star}\right)^{m}\int_{x_1}^{x_2}x^{m+1}e^{-x^2/2}\,dx\right), \quad (C.11)$$

where

$$\int_{0}^{y}x^{m+1}e^{-x^2/2}\,dx = (\text{sign } y)^m\,2^{m/2}\gamma\left(1+\frac{m}{2}, \frac{y^2}{2}\right), \quad (C.12)$$

and $\gamma(a, x) = \int_0^x t^{a-1}e^{-t}\,dt$ is the lower incomplete gamma function.

The formula (C.11) gives the expansion of the numerator (C.2) of v_{iodine} (27). Moreover, the denominator, which is the integral of the square of $\mathcal{F}_{\text{star}}'$ (C.1) can be computed by numerical integration using the same expansion. We observe numerically that the convergence of the expansion of v_{iodine}, using Eq. (C.11), is quite fast. In practice $K = 4$ already gives accurate results.

References

Albrecht, S., Winn, J. N., Johnson, J. A., et al. 2012, ApJ, 757, 18
Baranne, A., Queloz, D., Mayor, M., et al. 1996, A&AS, 119, 373
Beaugé, C. & Nesvorný, D. 2012, ApJ, 751, 119
Boisse, I., Bonfils, X., & Santos, N. C. 2012, A&A, 545, A109
Bundy, K. A. & Marcy, G. W. 2000, PASP, 112, 1421
Butler, R. P., Marcy, G. W., Williams, E., et al. 1996, PASP, 108, 500
Fabrycky, D. & Tremaine, S. 2007, ApJ, 669, 1298
Giménez, A. 2006, ApJ, 650, 408
Gray, D. F. 2005, The Observation and Analysis of Stellar Photospheres (New York, NY, USA: Cambridge University Press)
Hébrard, G., Bouchy, F., Pont, F., et al. 2008, A&A, 488, 763
Hirano, T., Suto, Y., Taruya, A., et al. 2010, ApJ, 709, 458
Hirano, T., Suto, Y., Winn, J. N., et al. 2011, ApJ, 742, 69
Holt, J. 1893, Astronomy and Astro-Physics, XII, 646
Kopal, Z. 1942, Proceedings of the National Academy of Science, 28, 133
Mandel, K. & Agol, E. 2002, ApJ, 580, L171
McLaughlin, D. B. 1924, ApJ, 60, 22
Nagasawa, M. & Ida, S. 2011, ApJ, 742, 72
Naoz, S., Farr, W. M., Lithwick, Y., Rasio, F. A., & Teyssandier, J. 2011, Nature, 473, 187
Ohta, Y., Taruya, A., & Suto, Y. 2005, ApJ, 622, 1118
Oshagh, M., Boisse, I., Boué, G., et al. 2012, ArXiv e-prints
Pál, A. 2012, MNRAS, 420, 1630
Pepe, F., Mayor, M., Galland, F., et al. 2002, A&A, 388, 632
Press, W. H., Teukolsky, S. A., Vetterling, W. T., & Flannery, B. P. 1992, Numerical recipes in C (2nd ed.): the art of scientific computing (New York, NY, USA: Cambridge University Press)
Queloz, D., Eggenberger, A., Mayor, M., et al. 2000, A&A, 359, L13
Rasio, F. A. & Ford, E. B. 1996, Science, 274, 954
Rossiter, R. A. 1924, ApJ, 60, 15
Santos, N. C., Mayor, M., Naef, D., et al. 2002, A&A, 392, 215
Simpson, E. K., Pollacco, D., Hébrard, G., et al. 2010, MNRAS, 405, 1867
Triaud, A. H. M. J. 2011, A&A, 534, L6
Triaud, A. H. M. J., Collier Cameron, A., Queloz, D., et al. 2010, A&A, 524, A25
Winn, J. N., Fabrycky, D., Albrecht, S., & Johnson, J. A. 2010, ApJ, 718, L145
Winn, J. N., Johnson, J. A., Fabrycky, D., et al. 2009, ApJ, 700, 302
Wu, Y. & Lithwick, Y. 2011, ApJ, 735, 109
Wu, Y. & Murray, N. 2003, ApJ, 589, 605